Received: 9 April 2021 | Revised: 27 July 2021 | Accepted: 27 July 2021

DOI: 10.1002/er.7163

RESEARCH ARTICLE

INTERNATIONAL JOURNAL OF ENERGY RESEARCH WILEY

Combined use of volumetric expanders and Scheffler receivers to improve the efficiency of a novel direct steam solar power plant

Paolo Iodice[1] | **Amedeo Amoresano**[1] | **Giuseppe Langella**[1] | **Francesco Saverio Marra**[2]

[1]Dipartimento di Ingegneria Industriale, Università degli Studi di Napoli Federico II, Naples, Italy

[2]Istituto di Ricerche sulla Combustione, Consiglio Nazionale delle Ricerche (IRC-CNR), Naples, Italy

Correspondence
Paolo Iodice, Dipartimento di Ingegneria Industriale, Università degli Studi di Napoli Federico II, Via Claudio 21 - 80125 Naples, Italy.
Email: paolo.iodice@unina.it

Summary

This research proposes an innovative solar thermal plant able to generate mechanical power through an optimized system of heliostats with Scheffler-type solar receivers coupled with screw-type steam expanders. Scheffler receivers appear to perform better than parabolic trough collectors due to the high compactness of the focal receiver, which minimizes convective and radiative heat losses even at high vaporization temperatures. At the same time, steam screw expanders are volumetric machines that can be used to produce mechanical power with satisfactory efficiency also by admitting two-phase mixtures and with further advantages compared to steam turbines: low working fluid velocities, low operating pressures, and avoidance of overheating. This study establishes a mathematical model to assess the energetic advantages of the planned solar thermal power system by evaluating the solar-to-electricity efficiency for different off-design working conditions. For this purpose, a numerical model on the Scheffler receiver is initially investigated, thus assessing all the energy losses which affect the heat transfer phase. A thermodynamic model is then developed to evaluate the energy losses and performance of the screw expander under real working conditions. Finally, parametric optimization of the solar energy conversion is performed in a wide range of operating conditions by establishing thermodynamic formulations related to the whole solar electricity generation system. Water condensation pressure and vaporization temperature are so optimized with respect to global energy conversion efficiency which, under the best operating conditions achieved in this research, rises from 10.9% to 14.4% with increasing solar irradiation intensity. Hence, the combined use of screw expanders and Scheffler receivers for solar thermal power system application can be a promising technology with advantages over parabolic dish concentrators.

Novelty statement

- This research proposes an innovative direct steam solar power plant based on an SRC, with water utilized as both heat transfer and working fluid, equipped with Scheffler solar receivers as a thermal source and screw expanders as work-producing devices.

- Technical studies and energy assessments of this kind of SEGS at part-load operation do not exist in scientific literature; after reviewing the literature, it was determined that volumetric expanders have been rarely combined with Scheffler receivers for solar thermal power system application.
- In effect, combined use of screw expanders and Scheffler-type solar concentrator in a direct steam solar power system represents a completely new plant configuration; however, as a promising DSG solar system, at present numerical model of this new sort of SEGS is lacked in literature and the optimum operating conditions have yet to be defined. For this reason, the chief objective of this paper is to define a first parametric optimization of all thermodynamic variables involved to maximize global efficiency of the proposed solar thermal power generation system for ordinary working conditions.

KEYWORDS

direct steam generation, Scheffler receivers, solar thermal power generation, steam screw expander

1 | INTRODUCTION

The combustion of fossil fuels is currently the chief contributor to air pollution and greenhouse gas emissions, which may be considered strictly responsible for global warming. Indeed, petroleum-based fossil fuels yet are the chief source of the global energy supply (around 80%).[1,2] Being motivated by such a crucial matter, the purpose of this new research was to design and optimize an innovative and flexible renewable energy power plant of reduced size and weight which can satisfy the energy demand of new municipal areas.

In this regard, although solar energy is typically the most plentiful and available among other types of renewable energy resources, solar thermal power system applications currently encounter several problems due to low energy density.[3] In effect, solar energy must be efficiently collected in concentrated solar power (CSP) systems to reach medium-high temperatures of suitable operating fluids combined with appropriate thermodynamic cycles. At present, low-medium temperature solar plants in real applications are often based on a Rankine cycle in combination with organic fluids to ensure high specific energy during the expansion phase even at reduced pressure levels.[4-6] However, such a solution also involves heat transfer between two fluids which can entail an exergetic destruction of the accessible thermal power. Moreover, solar thermal power plants based on organic Rankine cycles (ORCs) are also penalized by both poor thermodynamic performance at high temperatures and several problems concerning thermal instability, toxicity, and flammability of organic fluids. Under such conditions, solar energy may be difficult to exploit.[7-10]

All the environmental disadvantages associated with the use of organic fluids have thus stimulated the development of concentrated solar power (CSP) systems with direct steam generation (DSG).[11,12] Currently, solar electricity generation systems (SEGSs) with DSG are mainly based on linear Fresnel reflectors and parabolic trough collectors (PTCs) which represent a well-known technology in exploitation of solar power. Indeed, they supply almost 85% of the overall capacity of actual solar thermal power plants.[13-15] However, decreases in solar power collection efficiency with increasing vaporization temperatures can be pronounced in PTC receivers due to high convective and radiative heat losses.[16,17] In addition, since there is considerable variability in solar collector efficiency in such receivers, under particular weather conditions the reduction in solar irradiance can harm the mechanical power supplied by PTC-based power plants.[18]

Taking all the above aspects into account, this research proposes a novel direct steam solar power plant based on a steam Rankine cycle (SRC) which can be easily used for civil applications due to simple construction, low cost, and minimal environmental impact. This solar power system is equipped with Scheffler (SC) solar receivers as a thermal source and screw expanders (SEs) as work-producing devices, with water utilized as both heat transfer and working fluid.

To the best of our knowledge, to date there have been no energy evaluations or technical studies of this kind of SEGS at part-load operation; after reviewing the literature, it was determined that volumetric expanders have been rarely combined with Scheffler receivers for solar thermal power system applications.[19] In effect, combined use of SEs

and Scheffler-type solar concentrators in a direct steam solar power system represents a completely new plant configuration. However, as a promising DSG solar system, a numerical model of this new sort of SEGS equipped with Scheffler-type solar receivers and screw-type steam expanders is currently lacking in the literature and optimum operating conditions have yet to be defined.

For this reason, the chief objective of this study was to conduct a numerical optimization of the key thermodynamic parameters involved in order to maximize global efficiency of the proposed solar thermal power generation system for variable operating conditions. Hence, in this study, the energy performance of SC receivers and PTCs is compared, thereby assessing the technical viability of using such technology when installed in SE-based solar thermal electricity systems.

The SC solar paraboloid concentrator was introduced by the engineer Wolfgang Scheffler in 1980 as a unique fixed focus solar concentration device with the intent of application in developing nations.[20,21] Scheffler's idea was to create a high-quality reflector that required a reduced tracking mechanism and a simple structure so that it could be easily built, maintained, and operated at reasonable costs all over the world. In effect, SC receivers are designed to be a low-cost lightweight system: construction of each receiver costs less than €10 000, comprising the installation rates.[22,23] SC receivers also appear to perform better than PTCs due to the high compactness of the focal receiver which minimizes convective and radiative heat losses even at high vaporization temperatures.[24] Moreover, the decrease in solar power collection efficiency with decreasing solar radiation is less marked for SC receivers than in PTC receivers.

Although SC receivers were initially investigated for cooking, sterilization, and distillation applications (reaching steam temperatures up to 500°C),[25,26] some of these experimental results prove that the application field of such receivers can also be extended to DSG solar thermal power systems, by producing saturated steam to be expanded in turbines or volumetric expanders. In particular, in recent years, the advantages associated with the use of screw expanders for steam-liquid mixtures at not excessively high pressure or temperatures have been highlighted.[27,28]

For this reason, in the proposed SEGS, the dry saturated steam is initially obtained in the SC receiver and then flows into SEs to provide mechanical power. In this regard, although the SE-based SRC is currently mainly used in real applications for geothermal power generation and waste heat recovery, screw expanders are also promising for use in solar electricity generation systems, with several advantages over solar power systems which adopt steam turbines.[29-31] In effect, SEs prove to be more competitive than dynamic expanders, obtaining satisfactory heat-to-power conversion efficiencies under several operating conditions: when the net power is lower than a few MW, for vapor-liquid mixtures, at low-medium heat source temperatures, and at low-pressure ratios.[32-35]

However, when in real applications the actual pressure ratio rises overly compared to the built-in pressure ratio of such volumetric machines, the available enthalpy of high-temperature dry steam cannot be totally extracted through a sole SE, also entailing off-design working conditions.[36] Therefore, to obtain mechanical energy with acceptable efficiency, even on the working conditions of great difference between the SE built-in pressure ratio and the actual pressure ratio, this research assumes an innovative plant configuration based on two screw expanders coupled in tandem configuration, such that each volumetric machine can advantage from lower operating pressure ratios. That said, in the last few years, energetic assessments of two SEs combined in series have been performed for distributed solar thermal power generation. As described in recent publications, two screw expanders (coupled in a series) were installed in DSG power systems equipped with PTCs.[2,27,36]

However, unlike the above publications, in the present study, a new mathematical model for a Scheffler-type solar receiver coupled to SEs in tandem configuration is presented to investigate the energy assessment of a novel direct steam solar power plant in a broad range of fluctuating operating conditions. To the best of our knowledge, it is the first time that SEs coupled in series have been combined with Scheffler receivers in place of PTCs for solar thermal power system application. Thus, as a favorable solar electricity generation system, overall research on the off-design working conditions are essential. In this study, by determining the part-load models on both the SC receivers and the SEs, it will be possible to forecast the optimum operating conditions of the whole solar thermal power system under investigation.

That said, since both steam SEs and SC receivers operate under off-design operating conditions in several cases when installed in DSG solar systems, in this paper the energetic performance of the planned solar thermal power system is appraised with specific thermodynamic models under variable weather conditions and in a broad range of operating conditions. Thanks to such mathematical models, parametric optimization of the whole solar thermal power system is carried out via the following steps.

Initially, a thermodynamic model on the SC receiver is examined and proposed, thus revealing a variation in solar power collection efficiency with vaporization temperature and solar irradiance intensity. Through this model, all the energy losses influencing the heat transfer in the receiver are assessed (including convection, conduction, and

radiation losses). Subsequently, a numerical model is developed to describe the real expansion phase, appraising all the energy losses affecting energetic efficiency and performance of the screw expander under real working conditions. Finally, parametric optimization of the investigated DSG solar plant is performed with a macro balance approach, linking thermodynamic formulations fixed for the energetic appraisal of the whole solar power system with basic algorithms established for the SC receivers and the SE part-load behavior. For the purposes of parametric optimization of the designed solar power system under variable operating situations, these mathematical models are gathered in a computer package containing a set of MATLAB scripts. The independent variables of the models adopted for the numerical simulations (solar irradiance intensity, maximum steam pressure, and minimum steam pressure) are thereby enhanced with respect to the solar-to-electricity efficiency.

Hence, to maximize overall efficiency, parametric optimization is performed in a broad range of working conditions, also depending on season and weather conditions. Evaporation temperature is supposed to be fluctuating from 170°C to 300°C at intervals of 10°C, for different condensation pressure levels (100, 50, and 10 kPa), while solar irradiance intensity is assumed to range from 300 to 1000 W/m^2.

Knowledge of the impact of all these parameters in the global efficiency of the proposed solar power plant is essential for the further phase of the commercialization of this innovative system. Indeed, the numerical results attained in this research are investigated in-depth and may be considered useful for prompt delivery of the chief procedures for best harnessing of solar energy in low-medium Scheffler-based direct steam generation power plants equipped with screw expanders.

2 | NUMERICAL MODELS

2.1 | The Scheffler concentrator

2.1.1 | Scheffler reflector geometry

The surface of the SC reflector consists of a lateral section of a paraboloid, obtained by means of a generatrix of a circular section, which determines an elliptical perimeter of the frame. The focus remains positioned in front of the reflector and no shadows are projected onto the parabolic reflector from the receiver.

The section shown in Figure 1[37] shows the design methodology for the elliptical edge of the SC reflectors with respect to the equinox (the angle of solar inclination is $\delta = 0$). It starts from two assigned parameters, the aperture area of the reflector $A_{ap,\mathrm{ref}}$ and the focal distance of the parabola f. Hence, Figure 1 shows the parabola formed by the central section plane of the paraboloid from which the SC reflector was designed in the (x,y) plane, with axis y parallel to the solar rays; in this figure, $A_{ap,\mathrm{ref}}$ is the aperture area of the reflector and f is the focal distance of the parabola. The frame profile of the reflector on the (m,z') plane, with z' parallel to z and passing from point E_1, is also shown in Figure 1.

In this frame of reference, the equation of the parabola with focal distance f and vertex in the origin is given by Equation (1), while the equation of the section of the plane with slope β and intercept x_i can be written as in Equation (2):

$$x^2 = 4fy, \tag{1}$$

$$y = \tan\beta(x - x_i). \tag{2}$$

Let $E_1(x_1,y_1)$ and $E_2(x_2,y_2)$ be the intersection points of the inclined plane and of the parabola, respectively. The major and minor axis of the elliptical edge of the SC reflector can be given by Equations (3) and (4), respectively:

$$B_1 = \sqrt{(x_1 - x_2)^2 + (y_1 - y_2)^2}, \tag{3}$$

$$\mathrm{B}_2 = 2\sqrt{\frac{A_{ap,\mathrm{ref}}}{\pi}}. \tag{4}$$

Furthermore, B_2 is also the opening diameter of the opening circle and, for the specific geometry

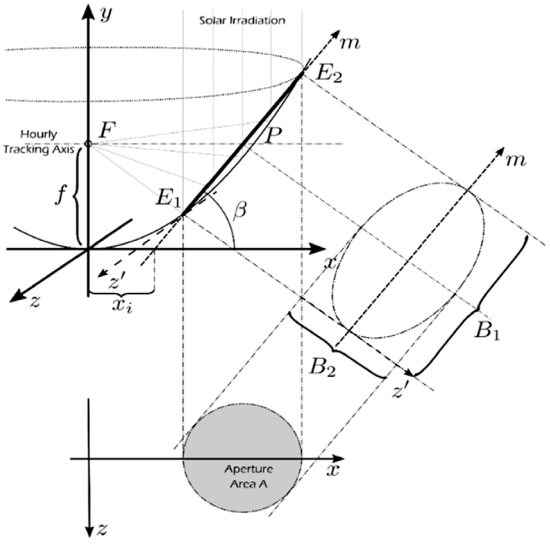

FIGURE 1 Geometrical parameters of the SC reflector[37]

indicated in Figure 1, B_1 can be also expressed as in Equation (5):

$$B_1 = \frac{B_2}{\cos\beta}. \tag{5}$$

By using Equations (1) to (5), the following relationships can be obtained:

$$x_1 = 2f\tan\beta + \frac{B_2}{2}; \quad y_1 = \frac{x_1^2}{4f}, \tag{6}$$

$$x_2 = 2f\tan\beta - \frac{B_2}{2}; \quad y_2 = \frac{x_2^2}{4f}, \tag{7}$$

$$x_i = f\tan\beta - \frac{B_2^2}{16f\tan\beta}. \tag{8}$$

The axis of rotation of the SC reflector for the hourly location of the sun is perpendicular to the axis of the parabola and passes through the focus of the parabola, intercepting the mirror parabola at point $P(2f,f)$.[20] Therefore, the rotation axis equation for time monitoring is given by Equation (9):

$$y = f. \tag{9}$$

Equation (1) for the parabola can be generalized to the following equation that follows the variation of the solar declination:

$$x^2 = 4f_n[y - (f - f_n)]. \tag{10}$$

In Equation (10), f is the focal length of the equinox parabola and f_n is the focal length of the parabola on the n-th day of the year which is derived by Equation (11), where δ_n is the angle of solar declination[38]:

$$f_n = f\left[1 - \cos\left(\frac{\pi}{2} - \delta_n\right)\right]. \tag{11}$$

2.1.2 | Determination of the image of the sun

Figure 2 illustrates the main quantities used to determine the image of the solar disk reflected on an infinitesimal area centered at point R of the SC concentrator. To determine the image of the reflector at the focal plane $y = f$, both nonparallel sun's rays and optical errors need to be accounted for.[38] Solar rays trace a cone with an angle $2\theta_s$, with $\theta_s \approx 0.27^\circ$ on the surface of the Earth.[39] The image on the focal plane perpendicular to the center line of the reflected ray will ideally assume an amplitude Δr given by Equation (12), where p is the distance from the generic point $R(x_R,y_R)$ on the surface of the concentrator to the focal point F as shown in Figure 2[40]:

$$\Delta r(x_R) = 2p(x_R) * \tan(\theta_s). \tag{12}$$

The image on the focal plane parallel to the aperture of the receiver cavity is:

$$w_R = \frac{\Delta r(x_R)}{\cos\left(\frac{\pi}{2} - \psi\right)}, \tag{13}$$

Actually, the optical imperfections of the reflector further enlarge the image and therefore reduce the performance of the system[41]: if a ray is incident with a cone

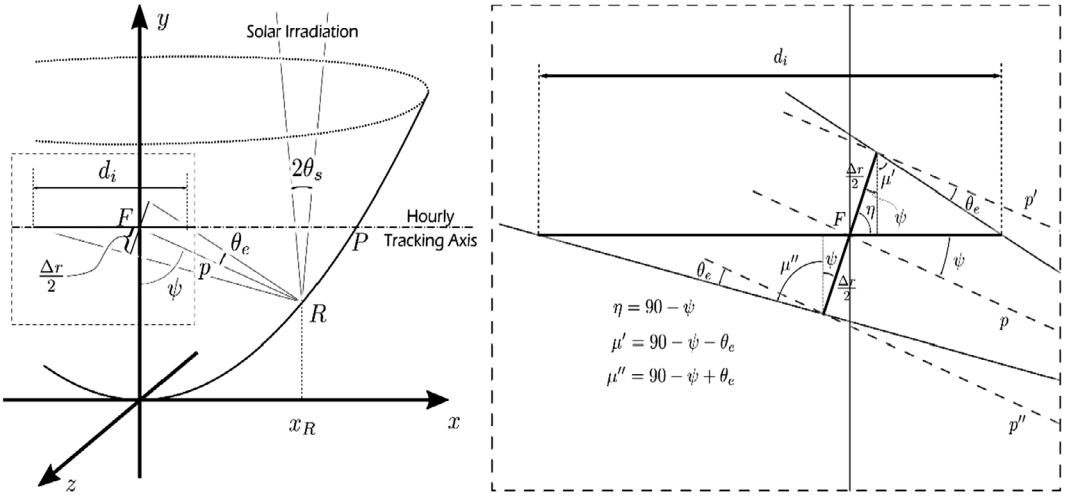

FIGURE 2 Reflection of a solar beam cone in the focal section in presence of imperfections (left). Magnification of the focal plane with the indication of the solar image (right)

angle of $2\theta_s$ it will be reflected with a cone angle of $2\theta_e$ with $\theta_e > \theta_s$. Several imperfections affect the collector systems and contribute to the spread of the beam. To express the cumulative effect of such errors, based on Gaussian approximation, the SD ν of all the errors (Equation [14]) includes the following imperfections[40]:

- errors due to the incorrect inclination of the parabolic mirror which occurred during manufacture, $\sigma_{\text{structure}}$;
- tracking errors due to sensors, σ_{sensor};
- errors due to tracking guides not perfectly aligned, σ_{drive};
- errors due to discrepancies in the mirror alignment of the receiver, σ_{align};
- errors due to variations in mirror reflectivity, σ_{refl};
- errors due to the width of the sun σ_{sun}.

$$\sigma_{\text{tot}} = \sqrt{(2\sigma_{\text{structure}})^2 + \sigma_{\text{sensor}}^2 + \sigma_{\text{drive}}^2 + \sigma_{\text{alignment}}^2 + (2\sigma_{\text{refl}})^2 + \sigma_{\text{sun}}^2}. \tag{14}$$

The effective opening of the focal image reflected at point R will thus be given by the following expression:

$$\Delta r(x_R) = 2p(x_R)\tan\left(\nu\frac{\sigma_{\text{tot}}}{2}\right). \tag{15}$$

Reversing Equation (15) and replacing Equations (12) and (13) with w_R substituted with the actual aperture of the cavity $d_{ap,\text{cav}}$, the expression for the SD ν at point x_R is obtained as in Equation (16):

$$\nu(x_R) = \frac{2}{\sigma_{\text{tot}}}\tan^{-1}\left(\frac{d_{ap,\text{cav}}\sin(\psi)}{2p(x_R)}\right). \tag{16}$$

In this equation, the normal distance $p(x_R)$ from the reflector to the focal point can be calculated as in Equation (17), with $y_R = x_R^2/4f$.

$$p = \sqrt{x_R^2 + (f - y_R)^2}. \tag{17}$$

2.1.3 | Receiver thermal model

In this study, after the receiver absorbs solar energy from the reflector, it transfers thermal energy to the working fluid. The use of a cavity receiver will be considered by adopting the receiver thermal model examined by Fraser.[42,43] In this model, the cavity receiver exploits solar energy from the reflector through a bundle of cylindrical tubes and, after being affected by heat losses, it collects the residual energy in the working fluid, as shown in Figure 3.

The energy balance of the receiver is written as in Equation (18), where the net heat available to transfer at the working fluid through the tubes, Q_{av}, can be considered as the difference between the heat collected in the cavity receiver, Q_{rec}, and all heat losses Q_{loss} which includes convection, conduction, and radiation losses.

$$\begin{aligned} Q_{av} &= Q_{\text{rec}} - Q_{\text{loss}} \\ &= Q_{\text{rec}} - Q_{\text{rad,ref}} - Q_{\text{rad,emi}} - Q_{\text{conv,nat}} - Q_{\text{conv,for}} \\ &\quad - Q_{\text{conv\_cond}}. \end{aligned} \tag{18}$$

Equation (19) estimates the amount of thermal energy captured in the cavity receiver, Q_{rec}.[38] In this equation, I_d is the direct irradiation of the sun (W/m^2), $A_{ap,\text{ref}}$ is the aperture opening area of the reflector (m^2), ρ

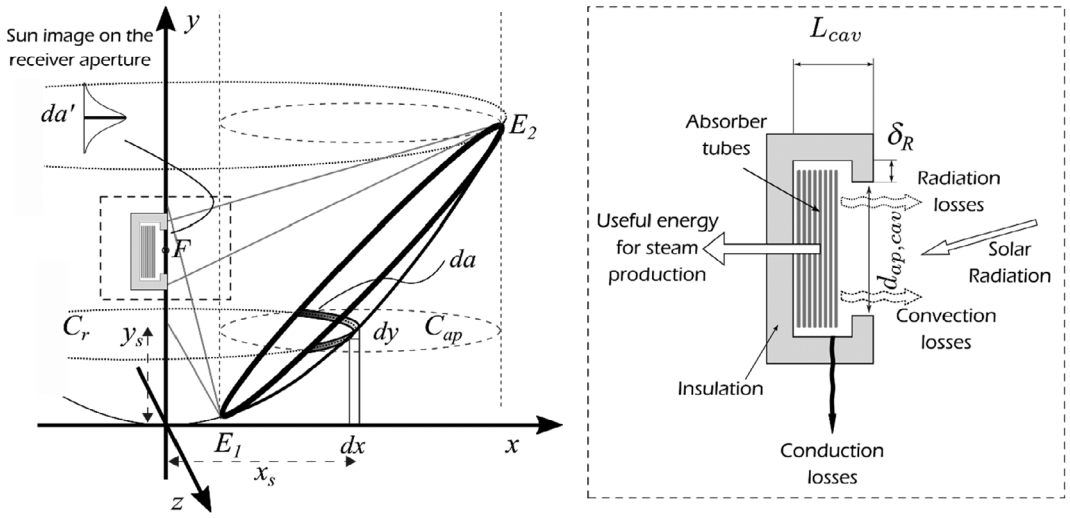

FIGURE 3 Scheme of the ensemble of reflector and receiver (left). Magnified view of the receiver following the model proposed by Fraser (right)[42]

(−) is the surface reflection coefficient and φ (−) is the interception factor. All terms of Equation (19) are known except the interception factor of the SC collector, which is given by the ratio between the power intercepted by the receiver $P_{\text{intercept,tot}}$ and the total power reflected by the collector $P_{\text{reflect,tot}}$, as explained in Equation (20).

$$Q_{\text{rec}} = I_d A_{ap,\text{ref}} \rho \varphi, \tag{19}$$

$$\varphi = \frac{P_{\text{intercept,tot}}}{P_{\text{reflect,tot}}} = \frac{\int_{E_1}^{E_2} I(a)\, da}{\int_{-\infty}^{\infty} I(a)\, da}. \tag{20}$$

To compute the integral at the numerator of Equation (20), it is advisable to determine the contribution of an element $dA_s = ds\, x_s\, d\theta$ of the mirror surface. dA_s is intercepted by the element dx along the x axis (see Figures 2 and 3) and the element of arc $x_s\, d\theta$ of the circumference C_r revolving the paraboloid at the same position and having limits on the elliptical border of the mirror (having coordinate $\pm z_b$ along the z axis), thus describing the shaded area da indicated in Figure 3.[44] Since $ds^2 = dx^2 + dy^2$, by substitution of the equation of the parabola:

$$ds = \sqrt{1 + \left(\frac{x}{2f}\right)^2}\, dx. \tag{21}$$

Coordinates $\pm z_b$ as a function of x_s are determined by intersecting the equation of the circumference C_r with radius x_s and the circumference C_{ap} of the sun interception area lying on the plane $y = y_s$ and having the center at point (x_c, y_s) and radius r:

$$\begin{cases} (x - x_c)^2 + z^2 = r^2 \\ x^2 + z^2 = x_s^2 \end{cases},$$

whose solutions are:

$$x_b = \frac{x_c^2 + x_s^2 - r^2}{2x_c}, \qquad z_b = \pm\sqrt{x_s^2 - x_b^2}.$$

Let $\theta_b = \arcsin(z_b / x_s)$. The integral at numerator of Equation (20) is then computed as:

$$\begin{aligned} \int_{E_1}^{E_2} I(a)\, da &= \int_{x_1}^{x_2} \int_{-z_b}^{+z_b} I(a)\, dA_s \\ &= \int_{x_1}^{x_2} \int_{-\theta_b}^{+\theta_b} I_d \cos(\psi/2) \sqrt{1 + \left(\frac{x_s}{2f}\right)^2}\, x_s\, d\theta dx, \end{aligned} \tag{22}$$

while the integral at denominator of Equation (20) is simply computed as $P_{\text{reflect,tot}} = I_d \pi r^2$.

When SC concentrators are considered, the maximum error of the polynomial approximation $I(a)$ can be assumed as a continuous function.[40] The normal distribution of the focal point radiation is given by Equation (23),[45] where $t = [1 + a\,\nu(x_s)/2]^{-1}$. The value of $\nu(x_s)$ depends on the diameter of the aperture of the receiver cavity, as expressed by Equation (16). All the coefficients appearing in the latter equation are reported in Table 1; this formula is determined when the rest *res* is considered negligible.

$$I(x) = I_d \left(1 - \frac{2}{\sqrt{2\pi}} e^{-\frac{\nu(x)^2}{8}} \left(b_1 t + b_2 t^2 + b_3 t^3 + b_4 t^4 + b_5 t^5\right) + 2\,\text{res}\right). \tag{23}$$

The interception factor φ for SC collectors is finally numerically obtained by replacing the geometric, statistical, and optical results (which depend on the dimensions and characteristics of the SC concentrator) in Equations (20) and (22), and discretizing the integral of Equation (22), thus obtaining Equation (24):

$$\varphi = \frac{\sum_{x_1}^{x_2} \sum_{-\theta_b}^{\theta_b} I(x_s) \cos(\psi/2) \sqrt{1 + \left(\frac{x}{2f}\right)^2}\, x_s \Delta x \Delta\theta}{I_d(\pi r^2)}, \tag{24}$$

Once the energy captured in the cavity is known, it is possible to estimate the losses of energy Q_{loss}, computing all the contributions reported in Equation (18). The heat loss due to the reflected radiation, $Q_{\text{rad,ref}}$, is calculated using Equation (25), where $(1 - \alpha_{\text{eff}})$ is the real reflectance of the cavity receiver computed from Equation (26) in which $A_{ap,cav}$ is the aperture opening area of the cavity.[38]

$$Q_{\text{rad,ref}} = (1 - \alpha_{\text{eff}})\, Q_{\text{rec}}, \tag{25}$$

TABLE 1 Coefficients of the normal distribution approximation

a	b_1	b_2	b_3	b_4	b_5
0.2316419	0.319381530	−0.356563782	1.781477937	−1.82125978	1.330274429

$$\alpha_{\text{eff}} = \left(\frac{\alpha_{\text{cav}}}{\alpha_{\text{cav}} + (1-\alpha_{\text{cav}}) \left(\frac{A_{ap,\text{cav}}}{A_{\text{cav}}} \right)} \right). \tag{26}$$

Radiation losses $Q_{\text{rad,emi}}$ due to the emitted radiation are calculated using Equation (27) where T_{amb} is the ambient temperature and T_{cav} is the temperature of the cavity.

$$Q_{\text{rad,emi}} = \varepsilon_{\text{eff}} \sigma^* A_{\text{int,cav}} \left(T_{\text{cav}}^4 - T_{\text{amb}}^4 \right). \tag{27}$$

In this expression, $A_{\text{int,cav}}$ is the internal surface of the cavity and the coefficient ε_{eff} is estimated by assuming $\varepsilon_{cav} = \alpha_{\text{cav}}$ and then determining the effective emission factor as suggested in Reference 46:

$$\varepsilon_{\text{eff}} = \left(\frac{(1-\varepsilon_{\text{cav}})}{\varepsilon_{\text{cav}} \left(1 + \frac{4L_{\text{cav}}}{2R_{\text{cav}}} \right)} + 1 \right)^{-1}. \tag{28}$$

Convection heat losses play an important role in the performance of a cavity receiver: they refer to the heat flow that comes out of the cavity opening due to the heating of the air inside it which rises by buoyancy or by pressure exerted by the wind. Convection heat losses are then divided into two parts: forced and natural convection losses. The natural convection heat losses for a cavity receiver, $Q_{\text{conv,nat}}$, can be expressed as in Equation (29). In this equation $A_{\text{int,cav}}$ is the internal surface of the cavity and $h_{\text{int,nat}}$ is the natural convection heat transfer coefficient that is estimated through the Nusselt number.

$$Q_{\text{conv,nat}} = h_{\text{int,nat}} A_{\text{int,cav}} (T_{\text{cav}} - T_{\text{amb}}). \tag{29}$$

The Nusselt number is correlated with the geometry and temperature of the cavity through the relationships expressed in Equations (30) and (31),[47] where $d_{ap,\text{cav}}$ is the aperture opening diameter of the cavity, θ is the inclination angle of the cavity and Gr is the Grashof number for natural convection heat transfer within the cavity (Equation (32). In Equation (32), g is the gravitational acceleration while β_{cav} and ν_{cav} are, respectively, the isobaric compressibility coefficient and the kinematic viscosity of the gas in the cavity receiver.

$$Nu_{\text{int,nat}} = 0.088\, \text{Gr}^{\frac{1}{3}} \left(\frac{T_{\text{cav}}}{T_{\text{amb}}} \right)^{0.18} \cos(\theta)^{2.47} \left(\frac{d_{ap,\text{cav}}}{d_{\text{cav}}} \right)^{m}, \tag{30}$$

$$m = -0.982 \left(\frac{d_{ap,\text{cav}}}{d_{\text{cav}}} \right) + 1.12, \tag{31}$$

$$Gr = \frac{g \beta_{\text{cav}} (T_{\text{cav}} - T_{\text{amb}}) d_{\text{cav}}^3}{\nu_{\text{cav}}^2}. \tag{32}$$

The forced convection losses can be estimated as the sum of two contributions, due to lateral wind and front wind components.[48,49] The heat loss coefficient due to lateral wind V_s, (expressed in W/m^{2}K), is computed as in Equation (33) and is independent of the orientation of the receiver opening. The heat transfer coefficient (W/m^{2}K) due to frontal winds V_f is computed as in Equation (34), where $f(\theta)$ is calculated in Equation (35). Thus, the forced convection losses, $Q_{\text{conv,for}}$, for a cavity receiver can be calculated as in Equation (36):

$$h_{\text{forced,side-on}} = 0.1967\, V_s^{1.849}, \tag{33}$$

$$h_{\text{forced,head-on}} = f(\theta)\, V_f^{1.401}, \tag{34}$$

$$f(\theta) = 0.163 + 0.749 \sin(\theta) - 0.502 \sin(2\theta) + 0.327 \sin(3\theta), \tag{35}$$

$$Q_{\text{conv,for}} = (h_{\text{forced,side-on}} + h_{\text{forced,head-on}}) A_{\text{int,cav}} (T_{\text{cav}} - T_{\text{amb}}). \tag{36}$$

Lastly, conduction heat losses are transferred through the inner walls of the cavity to the external ambient by a convection mechanism as described in Equation (37), where the convection heat transfer coefficient, termed $h_{\text{ext,cav}}$, involves both forced and natural convection coefficients, as expressed in Equation (38).[47] To compute the natural and forced convection coefficients ($h_{\text{ext,nat}}$ and $h_{\text{ext,for}}$) on the external surface of the cavity ($A_{\text{ext,cav}}$) when oriented vertically, the Nusselt number is calculated by Equations (39) and (40),[50] respectively.

$$Q_{\text{conv,cond}} = \frac{(T_{\text{cav}} - T_{\text{amb}})}{\frac{L}{k_{\text{int}} A_{\text{int,cav}}} + \frac{1}{h_{\text{ext,cav}} A_{\text{ext,cav}}}}, \tag{37}$$

$$h_{\text{ext,cav}} = \left(h_{\text{ext,nat}}^3 + h_{\text{ext,for}}^3 \right)^{\frac{1}{3}}, \tag{38}$$

$$Nu_{\text{ext,nat}} = 0.27 Re^{1/4}, \tag{39}$$

$$Nu_{\text{ext,for}} = 0.664 Re^{1/2} Pr^{1/3}. \tag{40}$$

The dimensions of the receiver should be chosen so as to minimize the losses, especially in radiative terms. For this purpose, starting from the choice of the aperture radius of the cavity $d_{ap,\text{cav}} = 0.30$ m, which ensures a high

interception factor $\varphi = 0.98$, the main coefficients of the terms appearing in Equations (26) and (28) were plotted as a function of the absorbance factor of cavity α_{cav} for different values of both cavity length L_{cav} and dimension δ_R (see Figure 3). Figure 4 reports a typical plot for two different values of δ_R.

From the analysis of these plots, for $\alpha_{cav} = 0.56$ as fixed by experimental measurements for a similar configuration,[19] the coefficients of radiative losses are always significant and appear minimized by reducing the cavity length L_{cav}, with no significant effects of the increased cavity aperture diameter $d_{ap,cav}$ (for fixed cavity diameter $d_{ap} = d_{ap,cav} + 2\delta_R$). It was concluded that, adopting realistic values of the physical coefficients, good performance of the Scheffler reflector-Fraser's cavity receiver is obtained by using the geometric parameters reported in Table 2.

Finally, the overall solar power collection efficiency η_{SOL} of SC receivers can be evaluated in Equation (41) as the share of solar irradiation $I_d \cdot A_{ap,ref}$ efficiently converted into net thermal power Q_{av} available to transfer to the working fluid. Hence, such efficiency considers all the possible thermal dispersions and optical losses of SC receivers as described in this section.

$$\eta_{SOL} = \frac{Q_{av}}{I_d \cdot A_{ap,ref}}. \tag{41}$$

2.2 | The screw expander: modeling and evaluation of overall efficiency

In reality, screw expanders are rotary-type power machines which offer some benefits in comparison with dynamic expanders: avoidance of overheating and satisfactory efficiency even when admitting working fluid both in two-phase conditions and at low enthalpy values. Besides, such volumetric engines can exploit enthalpy in working fluids with high levels of temperature and pressure, hence producing mechanical energy without the need of high fluid velocities. On the other hand, energy conversion in

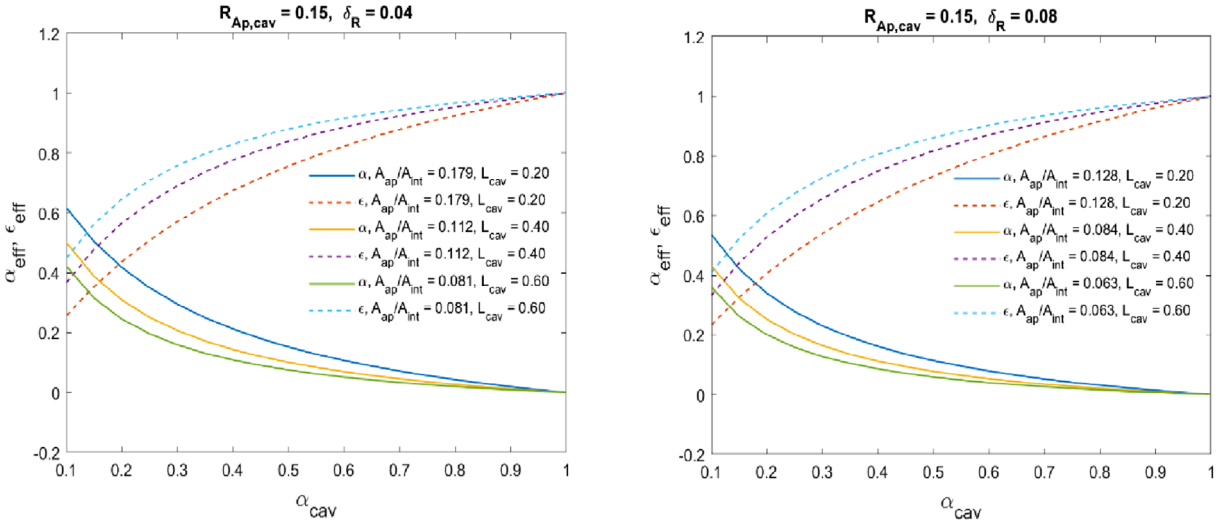

FIGURE 4 Coefficients of the radiative losses as a function of the geometrical and optical parameters of the receiver's cavity

TABLE 2 Selected physical and geometric values for evaluation of the solar power collection efficiency of the Scheffler reflector-Fraser cavity receiver system

Physical parameters	Value	Units	Geometric parameters	Value	Units
Mirror reflectance ρ	0.9	-	Capture area $A_{ap,ref}$	27.6	m^2
Cavity absorbance α_{cav}	0.56	-	Focal length f	2.1	m
Wind velocity	3	m/s	Cavity aperture diameter $d_{ap,cav}$	0.3	m
Optical errors deviation ν	0.012	rad	Cavity length L_{cav}	0.45	m
Latitude	41	deg	Cavity diameter d_{ap}	0.46	m
Ambient temperature	293	K	Cavity wall thickness	0.05	m
Insulation conductivity k_{ins}	0.09	W/mK	N. of absorber tubes	71	-
Air conductivity	0.029	W/mK	Absorber tubes diameter	0.0063	m

dynamic expanders can be negatively influenced by dynamic effects caused by excessive working fluid velocities.[2,27,33] Therefore, the risk of severe strains to the rotor blades resulting from dynamic effects during the expansion process of steam-liquid blends is appreciably lower for screw expanders than for dynamic expanders.

Under ideal operating conditions and when the actual expansion ratio $r_p = p_3/p_4$ is equal to the built-in expansion ratio $r_{p,b} = p_3/p_{4b}$, the theoretical isentropic work W_{Ti} can be calculated as in Equation (42). In this equation, p_3 is the vaporization pressure, p_4 is the actual exhaust pressure, and $p_{4,b}$ is the built-in exhaust pressure. In effect, under such ideal situations, the expansion phase of the working fluid follows the isentropic Equation $P{\cdot}v^k = \text{const}$ where k is the isentropic index:

$$W_{Ti} = -\int_3^4 v dp = -\int_3^4 [d(pv) - pdv] = p_3v_3 - p_4v_4 + \int_3^4 pdv = \frac{k}{k-1} p_3v_3\left(1 - r_p^{\frac{1-k}{k}}\right). \quad (42)$$

Nevertheless, under real operating conditions, there are several energy losses that can reduce the theoretical isentropic work output W_{Ti} delivered by a steady-flow screw expander, thus introducing the following three efficiencies[2,29,30]:

- η_{Th} is the theoretical efficiency which represents energy losses caused by high difference between the actual expansion ratio r_p and the built-in expansion ratio $r_{p,b}$ of the screw expander;
- η_D is the diagram efficiency which considers both energy losses from thermodynamic irreversibility and fluid leakage losses in the clearances between the helical rotors and machine casing (during admission and discharge phases);
- η_m is the SE mechanical efficiency that considers energy losses due to frictions from the helicoid lobed rotors, thus reducing the net work output.

The SE overall efficiency η_{SE} considers all these energy losses, as described in Equation (43).

$$\eta_{SE} = \eta_{Th} \cdot \eta_D \cdot \eta_m. \quad (43)$$

A key characteristic in SE design is the built-in volume fraction $r_{v,b} = v_{4,b}/v_3$ while working expansion ratio r_p can affect thermodynamic performance in real screw expander operations, as stated elsewhere.[30,31,35] The built-in volume ratio, which is assumed according to flow characteristics, geometric structure and rotation speed of the SE, must be kept on small values (generally ranging between 3 and 5.5 for commercial SEs) to maximize the induced input mass flow of steam before the high-pressure port is locked. Under the above operating conditions, the risks of fluid leakage losses are reduced by the high input mass flow rate. Furthermore, reducing the built-in volume fraction $r_{v,b}$ leads to less complex and bulky screw expanders.[51]

On the other hand, a reduced built-in volume ratio $r_{v,b}$ sets a low built-in pressure ratio ($r_{p,b} = {r_{v,b}}^k$). Thus, in real power plants, over-expansion operating conditions can occur when the real expansion ratios r_p exceed the fixed built-in pressure fraction $r_{p,b}$, thus involving off-design working conditions.[27,52] Besides, under such working situations, the outlet saturated steam would be discharged at too high a temperature, without exploiting the whole accessible enthalpy of expansion.[53]

Thus, energetic losses caused by ill-matching of the pressure ratio r_p in real operating conditions to the SE built-in pressure ratio $r_{p,b}$ reduce the theoretical isentropic work W_{Ti}, as expressed in Equation (44) by the theoretical efficiency η_{Th}. In this equation, W_{Td} represents the theoretical diagram work produced when the real expansion pressure p_4 deviates from the SE built-in discharge pressure p_{4b}.[2]

$$\eta_{Th} = \frac{W_{Td}}{W_{Ti}} = \frac{\frac{1}{k-1}p_3v_3\left(1 - {r_{p,b}}^{\frac{1-k}{k}}\right) + p_3v_3\left(1 - \frac{r_{p,b}^{\frac{1}{k}}}{r_p}\right)}{\frac{k}{k-1}p_3v_3\left(1 - r_p^{\frac{1-k}{k}}\right)} = \frac{\left(1 - r_{v,b}^{1-k}\right) + (k-1)\left(1 - \frac{r_{v,b}}{r_p}\right)}{k\left(1 - r_p^{\frac{1-k}{k}}\right)}. \quad (44)$$

As described in Equation (45), peak efficiency of the screw expander $\eta_{SE,p}$ is attained when the theoretical efficiency η_{Th} gets its peak value $\eta_{Th,p}$. Hence, if the maximum theoretical efficiency $\eta_{Th,p}$ is assumed as unitary, the SE total efficiency η_{SE} can be calculated as in Equation (46). Peak isentropic efficiency $\eta_{SE,p}$ then involves energy losses owing to fluid leakage losses, thermodynamic irreversibility and energy losses caused by mechanical frictions from the helical rotors.

$$\eta_{SE,p} = \eta_{Th,p} \cdot \eta_D \cdot \eta_m, \quad (45)$$

$$\eta_{SE} = \eta_{SE,p} \cdot \eta_{Th} = \eta_{SE,p} \cdot \frac{\left(1 - r_{v,b}^{1-k}\right) + (k-1)\left(1 - \frac{r_{v,b}}{r_p}\right)}{k\left(1 - r_p^{\frac{1-k}{k}}\right)}. \quad (46)$$

2.3 | Model validation

The validation process of the mathematical models proposed for the Scheffler-type solar receiver is established on the basis of the experimental values registered for the CNRS-PROMES receiver.[19,54,55]

To perform the numerical validation of the optical-geometric model, the values of interception factor φ computed by Equation (24) for the Scheffler mirror are compared in Figure 5 with the corresponding experimental values of a parabolic dish (PD).[55] The comparison shows that larger apertures are required with the Scheffler mirror to reach an equivalent interception factor with respect to the symmetric parabolic reflector, but with the advantage of moving the receiver away from the moving structure that allows for a much lighter and economical mirror and tracking system construction. However, as shown in Figure 5, the proposed geometric-optical model shows a good approximation of the WGA500 experimental results, presenting variations in interception factor between numerical results and test data always lower than 10% when the aperture diameter exceeds 0.17.

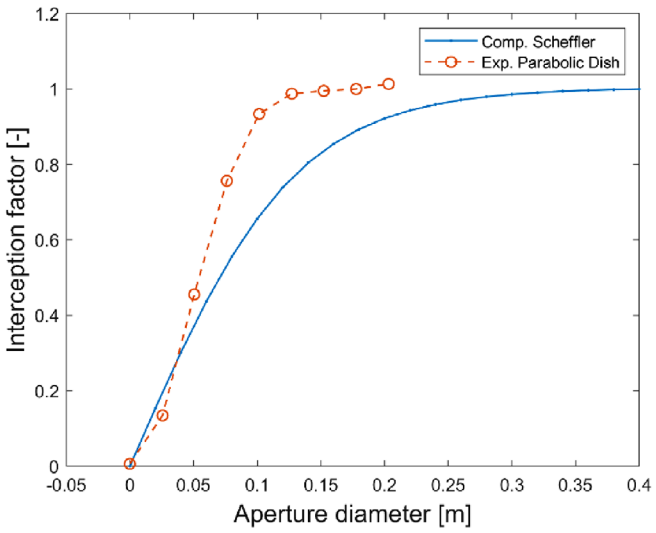

FIGURE 5 Comparison between the computed values of interception factor vs aperture diameter of the receiver cavity of the Scheffler system and experimental values obtained for a parabolic dish[55]

The experimental results reported for the 10 kW CNRS-PROMES system,[55] which is the most suitable for validating low-power receivers,[42] are also used to perform the numerical validation of the receiver thermal model adopted for the Scheffler reflector. The main computed heat losses achieved from simulation of the thermal model and the experimental results registered for the cavity receiver CNRS-PROMES system are compared in Table 3. However, conduction losses are not included in the comparison because, in the proposed thermal model, conduction heat losses transferred through the inner walls of the cavity to the external ambient by convection mechanism are included in the convection heat losses.[19]

For this comparison, Table 3 shows, in the first column (SC1 Mathematical model), the results from simulation of the thermal model when the receiver cavity is assumed to have geometric parameters as those fixed in Reference 55. The second column of Table 3 (SC2 Mathematical model) shows the numerical results achieved for the selected geometric parameters of the Scheffler reflector under investigation, which are already reported in Table 2. Comparison is not immediate because of the different purpose of the two systems, leading to different cavity equilibrium temperature (322°C and 306°C for SC, 850°C for PD). However, these results show the sensitivity of the model and the ability to reproduce the correct trends with the variation of the geometric parameters. Consequently, the values of solar power collection efficiency computed with the optical-geometric model and the receiver thermal model, which will be shown in the next sections, prove consistent with the experimentally determined efficiencies for Scheffler concentrators reported elsewhere.[22,23,26]

Variations in the SE global efficiency with pressure ratio obtained from the thermodynamic model will be explored in-depth in the next sections However, the validation process of the proposed model is performed by

TABLE 3 Comparison between the experimental results[55] and the proposed model

	SC1 Mathematical model (kW)	SC2 Mathematical model (kW)	PD experimental results (kW)[55]
Captured solar power	48.02	48.02	48.02
Intercepted thermal power	35.30	43.64	37.75
Heat loss due to emitted radiation	0.49	5.77	2.39
Heat loss due to reflected radiation	18.17	3.53	1.71
Heat loss due to convection	0.58	0.40	1.98
Net thermal power	16.05	33.66	31.67

considering the experimental and numerical results reported in previous scientific publications.[33,36,56,57] In this regard, predicted data are in good agreement with the experimental results shown in Figure 6[56]; in effect, numerical results obtained from our simulations show maximum variations which are always lower than 5% when compared to the average experimental data registered for pressure ratios ranging between 3.5 and 6.5. Besides, the predicted isentropic efficiency values of the screw expander, for pressure ratios ranging between 8 and 27, are within ±5% also when compared to experimental data reported in Reference 57.

Numerical results obtained from the proposed thermodynamic model are in perfect agreement also with the SE over-expansion model established in Reference 33. In particular, when the built-in volume ratio $r_{v,b}$ is set to 5, for both models the SE overall isentropic efficiency declines from 73% to 61% under actual pressure ratios r_p increasing from 9 to 30.

The energy assessment of a DSG solar power system using PTCs and two SEs in a tandem configuration was performed in a previous publication for different $r_{v,b}$ combinations of SEs.[36] For inlet and outlet pressures preventively set at 10 bar and 0.1 bar, the SRC efficiency of 18.49% was reached when the built-in volume ratios $r_{v,b}$ of the two screw expanders were fixed to 3 and 7. Instead, in the proposed thermodynamic model, when the built-in volume ratio is set at 5 for both screw expanders, the SRC efficiency is 19.33% under similar operating conditions (ie, $r_p = 100$), thus showing good agreement.

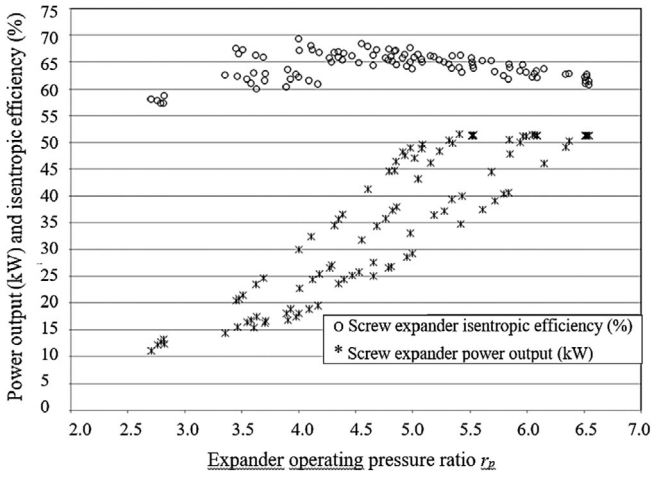

FIGURE 6 Test results of variations in screw expander isentropic efficiency with pressure ratio[56]

3 | SYSTEM DESCRIPTION AND GLOBAL ENERGY CONVERSION EFFICIENCY OF THE SOLAR THERMAL POWER SYSTEM

The plant design analyzed in this research is based on two screw expanders (as work-producing devices) in a tandem configuration in a solar thermal power system adopting SC receivers as a thermal source, with water used as both heat transfer and working fluid. The schematic diagram of the DSG solar power plant in question is shown in Figure 7. In the CSP-SRC plant analyzed in this study, the expansion process starts in the screw expander SE_1 where the dry saturated steam expands from *3* to *3′* and after, flowing into the second screw expander (SE_2), it continues to expand from *3′* to discharge line *4*, thereby providing a further rate of mechanical power. After the steam has been exhausted by SE_2, it

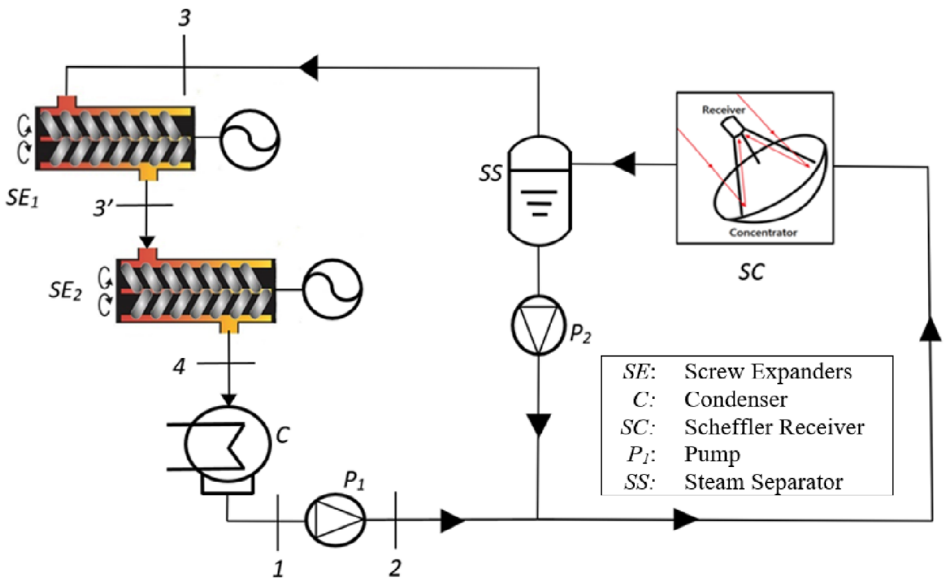

FIGURE 7 Plant configuration of the CSP-SRC plant with DSG equipped with Scheffler solar receivers (*SC*) and screw expanders (SE_1 and SE_2)

flows (from *4* to *1*) into condenser *C* to obtain saturated liquid which is then pressurized (from *1* to *2*) by pump P_1 toward the Scheffler receiver (*SC*). Lastly, the saturated steam released by the Scheffler receiver is gathered in the steam separator unit (*SS*) hence obtaining dry saturated steam.

As is clear from Figure 7, two steam screw expanders are combined in tandem configuration to decrease the operating expansion ratios r_p of both SEs, thus wholly exploiting the accessible enthalpy of expansion that can be obtained from the high-temperature saturated steam. In reality, as already examined in the previous sections, the built-in pressure ratio $r_{p,b}$ of screw expanders may frequently be lower than the operating expansion ratio in a real DSG solar power plant, hence affecting off-design operating conditions. In effect, global efficiency of screw expanders (Equation [46]) gradually declines when the operating pressure ratio grows overly compared to the set SE built-in expansion ratio. Hence, by assuming this plant layout, the whole operating pressure ratio can be shared on two volumetric machines, such that both screw expanders benefit from smaller operating pressure ratios r_p.

The steam Rankine cycle efficiency η_{SRC} of the solar power plant under examination is expressed in Equation (47). In this equation, the power of the Rankine cycle P_{SRC} is assumed as the difference between the power delivered by the SEs (P_{SE}) and the power needed by the pump (P_p), η_{SE} represents the SE total efficiency (exposed in Equation [46]) and Q_{av} is the heat transfer rate. Clearly, η_p is the pump efficiency, h_1 is the water enthalpy at the pump inlet and $h_{2,is}$ is the isentropic enthalpy at the pump outlet. Also, h_3 is the water enthalpy at the inlet of the first screw expander SE_1 and $h_{4,is}$ is the isentropic enthalpy of water at the outlet of the second screw expander SE_2. Evidently, the enthalpy levels of all these state points depend on the particular steam Rankine cycle.

$$\eta_{\mathrm{SRC}} = \frac{P_{\mathrm{SRC}}}{Q_{av}} = \frac{P_{SE} - P_P}{Q_{av}} = \frac{(h_3 - h_{4,is}) \cdot \eta_{SE} - (h_{2,is} - h_1)/\eta_p}{(h_3 - h_2)}. \tag{47}$$

In Equation (48), the percentage of solar irradiation intensity $I_d \cdot A_{ap,ref}$ efficiently converted into output power by the proposed solar power system ($P_{\mathrm{NET}} = P_{\mathrm{SRC}} \cdot \eta_{\mathrm{mec}}$) is assessed by the solar thermal power efficiency η_G. In the above equation, η_{SOL} is the solar power collection efficiency (Equation [41]) and η_{mec} is the mechanical efficiency of the DSG power plant under investigation which also includes generators efficiency. Hence, this solar-to-electricity efficiency η_G can be assumed as the global energy conversion efficiency of the planned solar power plant.

$$\eta_G = \frac{P_{\mathrm{NET}}}{I_d \cdot A_{ap,\mathrm{ref}}} = \eta_{\mathrm{SOL}} \cdot \eta_{\mathrm{SRC}} \cdot \eta_{\mathrm{mec}} = \frac{Q_{av}}{I_d \cdot A_{ap,\mathrm{ref}}} \left[\frac{(h_3 - h_{4,is}) \cdot \eta_{SE,p} \dfrac{\left(1 - r_{v,b}^{1-k}\right) + (k-1)\left(1 - \frac{r_{v,b}}{r_p}\right)}{k\left(1 - r_p^{\frac{1-k}{k}}\right)} - \frac{(h_{2,is} - h_1)}{\eta_p}}{(h_3 - h_2)} \right] \eta_{\mathrm{mec}}. \tag{48}$$

4 | ANALYSIS OF RESULTS AND DISCUSSION

4.1 | Model variables

Parametric optimization of the planned DSG solar system is achieved in a broad range of operating situations, by linking thermodynamic formulations fixed for the energetic appraisal of the whole power system assumed as a black-box (as described in Section 3), with algorithms obtained both for the SC receivers (Section 2.1) and the SE part-load behavior (Section 2.2). By adopting such numerical models and having fixed all chief thermodynamic factors for mathematical simulations (Table 4), the global energy conversion efficiency η_G of this solar power system can then be calculated for various combinations of vaporization temperature, condensation pressure, and solar irradiation intensity, hence forecasting the optimum operating conditions. In detail, evaporation temperature is supposed to be fluctuating from 170°C to 300°C (at intervals of 10°C) while condensation pressure (back pressure p_4 of discharge line) is assumed equal to 10, 50, and 100 kPa, under different irradiance values from 300 to 1000 W/m^2 at intervals of 100 W/m^2 (depending on time, season, and weather conditions). For the purposes of the parametric optimization established on the planned power system under fluctuating working conditions, the whole calculation procedure is implemented in a specific MATLAB model, such that enthalpy values at each state point were calculated for each vaporization temperature, when condensation pressure p_4 is set to 100, 50, and 10 kPa, as shown in Tables 5 to 7, respectively.

TABLE 4 Fixed thermodynamic parameters

Terms	Value
$r_{v,b}$: SE built-in volume ratio	5
η_p: pump efficiency	0.80
$\eta_{\mathrm{SE},p}$: SE peak efficiency	0.75
k: isentropic index	1.15
η_{mec}: mechanical efficiency	0.95

TABLE 5 Enthalpy values at each state point calculated against vaporization temperatures when condensation pressure is set at 100 kPa

Vaporization temperature T_3 (°C)	Vaporization pressure P_3 (MPa)	SE_1 inlet enthalpy h_3 (kJ/kg)	SE_2 outlet enthalpy h_4 (kJ/kg)	Condenser outlet enthalpy h_1 (kJ/kg)	Pump outlet enthalpy h_2 (kJ/kg)
170	0.79	2767.8	2587.0	419.0	419.7
180	1.00	2777.1	2541.6	419.0	420.0
190	1.25	2785.2	2503.0	419.0	420.2
200	1.55	2791.9	2469.6	419.0	420.5
210	1.90	2797.2	2440.3	419.0	420.9
220	2.31	2800.9	2414.2	419.0	421.3
230	2.79	2802.9	2390.6	419.0	421.8
240	3.34	2803.0	2368.9	419.0	422.4
250	3.97	2801.0	2348.3	419.0	423.1
260	4.68	2796.7	2328.5	419.0	423.8
270	5.49	2789.8	2309.0	419.0	424.6
280	6.40	2780.0	2289.1	419.0	425.6
290	7.43	2766.9	2268.5	419.0	426.7
300	8.57	2749.9	2246.6	419.0	427.8

TABLE 6 Enthalpy values at each state point calculated against vaporization temperatures when condensation pressure is set at 50 kPa

Vaporization temperature T_3 (°C)	Vaporization pressure P_3 (MPa)	SE_1 inlet enthalpy h_3 (kJ/kg)	SE_2 outlet enthalpy h_4 (kJ/kg)	Condenser outlet enthalpy h_1 (kJ/kg)	Pump outlet enthalpy h_2 (kJ/kg)
170	0.79	2767.8	2451.2	340.5	341.3
180	1.00	2777.1	2421.4	340.5	341.5
190	1.25	2785.2	2396.0	340.5	341.8
200	1.55	2791.9	2374.1	340.5	342.1
210	1.90	2797.2	2354.7	340.5	342.4
220	2.31	2800.9	2337.3	340.5	342.9
230	2.79	2802.9	2321.3	340.5	343.4
240	3.34	2803.0	2306.2	340.5	343.9
250	3.97	2801.0	2291.6	340.5	344.6
260	4.68	2796.7	2277.0	340.5	345.3
270	5.49	2789.8	2262.0	340.5	346.1
280	6.40	2780.0	2246.3	340.5	347.1
290	7.43	2766.9	2229.3	340.5	348.1
300	8.57	2749.9	2210.7	340.5	349.3

4.2 | Solar collector efficiency

The equilibrium temperature of the cavity is established by balancing the energy received by the reflector, the energy lost in the environment and the energy transferred to the water for steam generation. The useful heat Q_{av} left in the cavity, calculated in Equation (18), is transferred to the working fluid through the walls of the absorber tubes. It is calculated as shown in the following equation:

$$Q_{av} = h_{p,w} A_p (T_{\text{cav}} - T_w), \tag{49}$$

where:

TABLE 7 Enthalpy values at each state point calculated against vaporization temperatures when condensation pressure is set at 10 kPa

Vaporization temperature T_3 (°C)	Vaporization pressure P_3 (MPa)	SE_1 inlet enthalpy h_3 (kJ/kg)	SE_2 outlet enthalpy h_4 (kJ/kg)	Condenser outlet enthalpy h_1 (kJ/kg)	Pump outlet enthalpy h_2 (kJ/kg)
170	0.79	2767.8	2284.9	191.8	192.6
180	1.00	2777.1	2276.2	191.8	192.8
190	1.25	2785.2	2268.0	191.8	193.1
200	1.55	2791.9	2260.9	191.8	193.4
210	1.90	2797.2	2254.2	191.8	193.7
220	2.31	2800.9	2247.9	191.8	194.1
230	2.79	2802.9	2241.5	191.8	194.6
240	3.34	2803.0	2234.8	191.8	195.2
250	3.97	2801.0	2227.5	191.8	195.8
260	4.68	2796.7	2219.4	191.8	196.5
270	5.49	2789.8	2210.1	191.8	197.3
280	6.40	2780.0	2199.4	191.8	198.3
290	7.43	2766.9	2186.9	191.8	199.3
300	8.57	2749.9	2172.1	191.8	200.4

- $h_{p,w}$ is the global heat transfer coefficient between the cavity and the water;
- A_p is the surface extent of the pipes;
- T_w is the temperature of the water.
- T_{cav} is the temperature of the cavity.

It is here assumed that an appropriate amount of liquid water circulates in the circuit, such that the maximum fraction of steam in the boiling water x_s never exceeds the 10%, all this to ensure that the conditions of nucleate boiling occur inside the tubes. As is well known, this is the best heat exchange condition for boiling water allowing a heat transfer coefficient inside the tube up to 10 000 W/m^2K. Considering the high temperature of the chamber which radiates towards the pipes and the high conductivity of the pipes themselves, the global heat transfer coefficient between cavity and water can be prudently assumed equal to 3500 W/m^2K.

The difference of temperature between the inlet and outlet of the heat exchanger in the cavity, respectively T_{in} and T_{out}, is small: the inlet temperature is the weighted average of the condensed fraction of vapor used in the SE, which is at most 10% of the whole amount of water, and 90% of boiling water at the saturation temperature, while T_{out} will not exceed the saturation temperature. After a small portion of the heat exchanger working as economizer, the boiling point is reestablished and the temperature will keep constant at the saturation temperature, $T_{\text{out}} = T_w = T_{\text{sat}}$ for the fixed pressure. Boiling water will then flow in almost the entire length of the exchanger. The temperature T_{cav} is unknown. Therefore, as initial guess is assigned at the beginning of the computation to determine all the heat losses, Q_{loss}, a new value is then computed by solving Equation (49). This value is adopted to estimate the water flux allowed to keep constant the end fraction of steam to the assigned x_s. Indeed, the available heat is used to raise the water temperature to boiling point and then to supply the required latent heat, as expressed in Equation (50), which can be solved in the unknown $\dot{m}_w$.

$$Q_{av} = \dot{m}_w c_{v,w} (T_{sat} - T_{in}) + \dot{m}_w x_s h_l. \tag{50}$$

This procedure is iterative, as the entire computation need to be repeated with the new values of T_{cav} and $\dot{m}_w$. A relaxation parameter of 0.8 ensure convergence in very few iterations. T_{in} was fixed at 0.95 T_{sat}. Properties of water steam are computed by linear interpolation of NIST steam data tables.

Finally, considering the numerical models described in Section 2.1, which evaluate all the possible thermal dispersions and optical losses of a SC receiver, the thermal power transferred to the fluid in the concentrator was calculated by means of a code on the MATLAB program. According to Equation (41), in Figure 8 such net thermal power Q_{av} is compared to the solar radiation $I_d \cdot A_{ap,\text{ref}}$ arriving on the receiver, thereby obtaining variations in collection efficiency η_{SOL} of SC receivers with vaporization temperatures (ranging between 170°C and 300°C) under several solar radiation intensities. It is evident that such solar power collection efficiency η_{SOL} always declines with vaporization temperatures T_3 in the solar irradiation range between 300 and 1000 W/m^2.

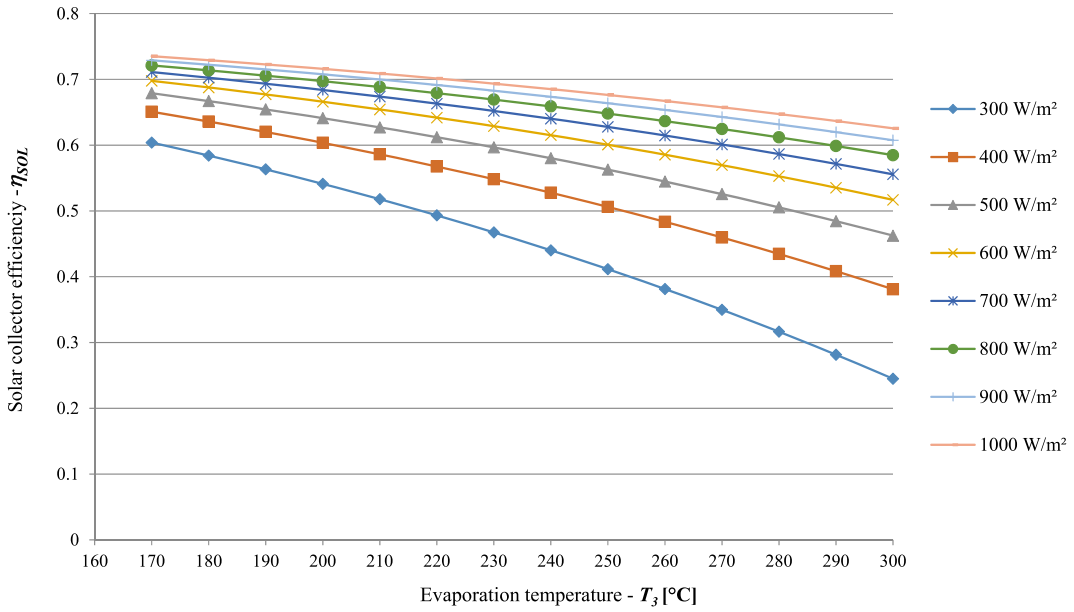

FIGURE 8 Variations in solar collector efficiency of SC receivers with vaporization temperature and solar irradiation intensity

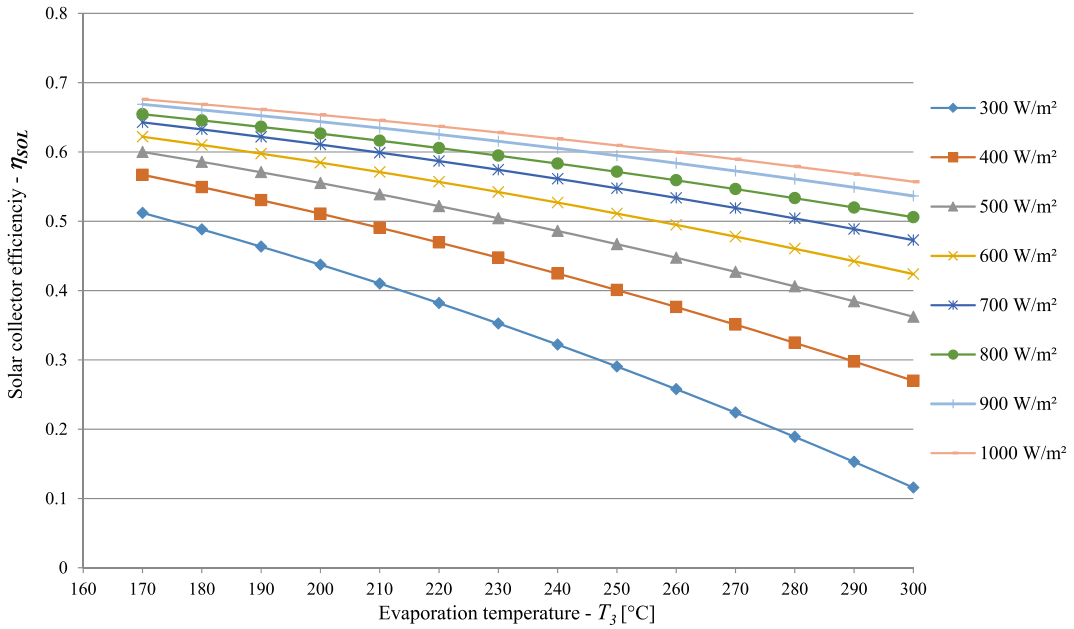

FIGURE 9 Variations in solar collector efficiency of PTC receivers with vaporization temperature and solar irradiation intensity

To better show the energetic advantages of the proposed SC receivers, the solar collector efficiencies η_{SOL} of SC receivers can be compared with those of common PTC receivers in the same ranges of evaporation temperature and solar irradiation intensity. In Figure 9 the PTC solar power collection efficiencies are assessed against the vaporization temperature under growing solar irradiation intensity. Thus, by comparing the solar collector efficiencies η_{SOL} of Figures 8 and 9, SC receivers appear to perform slightly better due to higher compactness of the focal receiver compared to the linear collector of PTC receivers, thus minimizing the heat exchange area with the environment. In fact, the efficiency of SC receivers remains sufficiently high even at high vaporization temperatures, while in the PTCs the decay in the efficiency η_{SOL} is more pronounced because convective and radiative heat losses become more considerable with increasing temperature.

In addition, careful analysis of the results shown in these last two figures reveals that the variability of the solar collector efficiency with solar radiation is albeit

slightly less wide for the SC receivers in comparison with PTC receivers. This aspect somewhat mitigates the negative effect that variations in solar irradiance intensity can have on the mechanical power supplied by solar power systems adopting SC receivers compared to similar DSG solar power plant adopting parabolic trough collectors.

4.3 | Screw expander efficiency and steam Rankine cycle efficiency

In Figure 10, the efficiency η_{SE} of screw expanders vs evaporation temperature is obtained by using Equation (46) (which reveals the SE overall efficiency calculated against the working pressure ratio r_p), when the built-in volume ratio $r_{v,b}$ is equal to 5 (as fixed in Table 4) and under condensation pressures p_4 fixed to 10, 50, and 100 kPa. As specified in the previous section, the mismatch of the working expansion ratio r_p with the built-in pressure ratio $r_{p,b}$ entails two reverse effects which cause poor energetic performance in screw expander operation: the blowback effect and the blowdown effect.[2,51] For the power plant presented in this paper, a decline in SE efficiency η_{SE} is clear in Figure 10 with growing vaporization temperature and when real exhaust pressure p_4 cuts from 100 kPa bar to 10 kPa (over-expansion working situations, $r_p > r_{p,b}$).[52] Basically, with declining condensation pressure and growing vaporization temperature, the resultant working pressure ratio r_p progressively rises compared to $r_{p,b}$, hence affecting off-design operating conditions due to the blowback effect.[35]

Furthermore, on examining Figure 10, a significant reduction in SE efficiency η_{SE} is also clear when under-expansion working situations occur, that is $r_p < r_{p,b}$. In effect, in such a case (exhaust pressure assumed equal to 100 kPa and declining vaporization temperature), the resultant working pressure ratio decreases excessively compared to the built-in pressure ratio $r_{p,b}$, then involving off-design working conditions caused by the blowdown effect.[34,35] Indeed, the efficiency of both screw expanders is known to reach its peak value when the working expansion ratio matches the built-in pressure ratio.[35]

The heat-to-power conversion efficiency η_{SRC} depends on SE efficiency η_{SE} and actual pressure ratio r_p, as expressed in Equation (47). In Figure 11, the steam Rankine cycle efficiency η_{SRC} is computed against vaporization temperature for exhaust pressure set to 10, 50, and 100 kPa. Under high condensation pressures (around 1 bar) and reduced vaporization temperatures, this efficiency is evidently lower owing to a reduction both in SE efficiency η_{SE} (caused by under-expansion situations) and in obtainable enthalpy of expansion.[27,52]

However, when condensation pressure is set to 100 kPa, the efficiency η_{SRC} always grows with vaporization temperature rising from 170°C to 300°C. Therefore, under this operating condition, growth in the obtainable enthalpy of expansion with an increasing vaporization temperature can prevail over a decrease in efficiency of the steam SEs caused by over-expansion working conditions. By contrast, when condensation pressure is

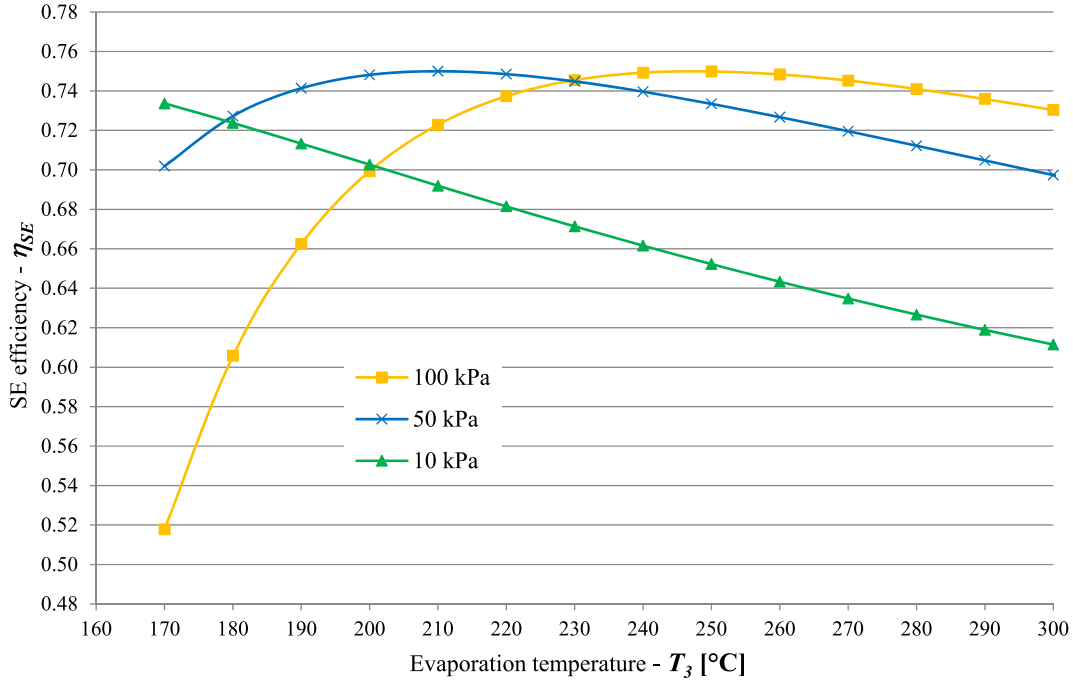

FIGURE 10 SE efficiency calculated against vaporization temperature under fixed condensation pressures

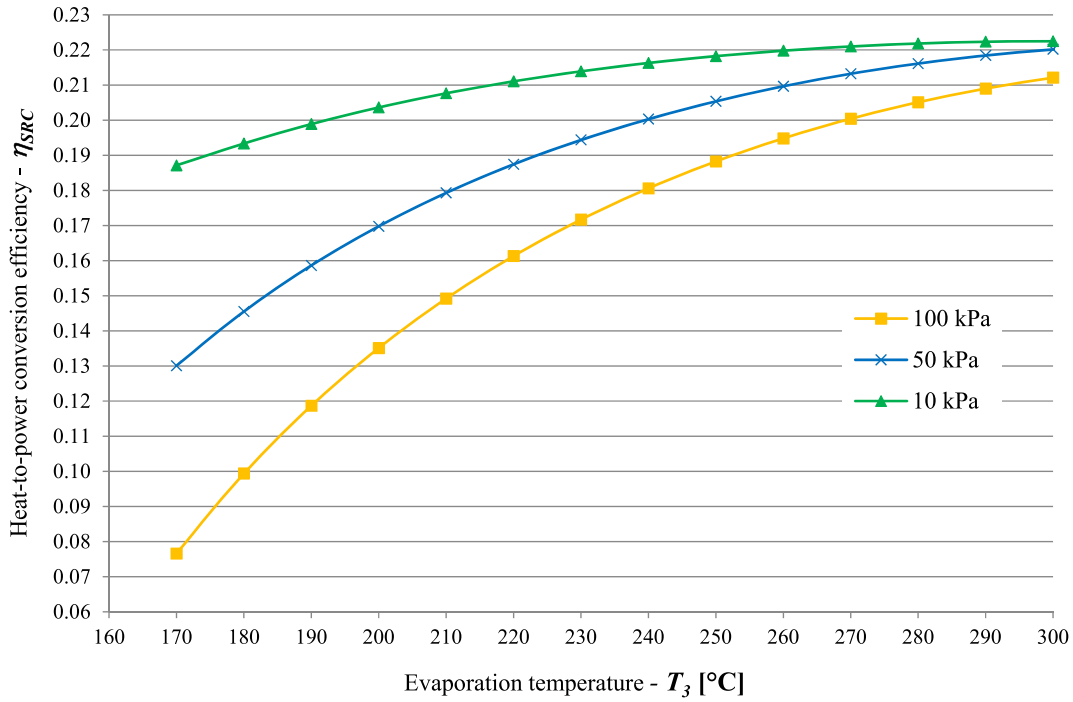

FIGURE 11 Steam Rankine cycle efficiency computed against vaporization temperature for fixed condensation pressures

assumed equal to 10 kPa, the efficiency η_{SRC} becomes nearly constant with vaporization temperatures higher than 260°C since, in this specific case, a decline in SE efficiency as vaporization temperature growths (due to severe over-expansion conditions) equalizes a growth in the accessible enthalpy of expansion.

4.4 | Solar-to-electricity efficiency

In this subsection, the proposed solar power system is examined in-depth and is optimized energetically. Hence, the optimum inlet temperatures T_3 which lead to maximum energetic efficiency are calculated for every solar irradiation intensity and condensation pressures p_4. For this purpose, it is first crucial to show the impact of all these parameters on the solar-to-electricity efficiency η_G of the whole solar thermal power plant. Such global energy conversion efficiency η_G in all possible operating conditions was calculated according to Equation (48). Thus, it depends on solar collector efficiency of the receivers η_{SOL}, steam Rankine cycle efficiency η_{SRC} (also including the screw expander efficiency η_{SE}) and mechanical efficiency η_{mec} which includes frictions from all the moving parts (alternator plus other mechanical frictions). Therefore, having fixed the mechanical efficiency η_{mec} and the SE built-in volume ratio as in Table 4, this overall efficiency can be calculated for various combinations of vaporization temperature, condensation pressure, and solar irradiation intensity.

Thus, for the planned solar power plant, by assuming Equation (48), variations in solar-to-electricity efficiency η_G with solar irradiance and vaporization temperature are assessed under condensation pressures supposed equal to 100, 50, and 10 kPa, in Figure 12 to 14, respectively. Hence, the results displayed in these figures give the exact impact of the optimization parameters on the global energy conversion efficiency.

When condensation pressure p_4 is set at 100 and 50 kPa, Figures 12 and 13, respectively, show that low evaporation temperatures always produce lower solar-to-electricity efficiencies η_G in comparison with its maximum values because a reduction in the steam Rankine cycle efficiency η_{SRC} with a decreasing evaporation temperature (as described in Figure 11 under the same condensation pressures p_4) overcomes a rise in solar collector efficiency η_{SOL}. Under these two particular condensation pressures, in fact, for low vaporization temperatures T_3 and for each solar radiation, the solar-to-electricity efficiency η_G is reduced by both a reduction in obtainable enthalpy of expansion and an increase in energy losses resulting from excessive under-expansion conditions (blowdown effect) which can affect reduced thermodynamic performance in real screw expander operations.[52]

By contrast, when the condensation pressure is assumed equal to 10 kPa and for each solar irradiance intensity, the global efficiencies η_G shown in Figure 14

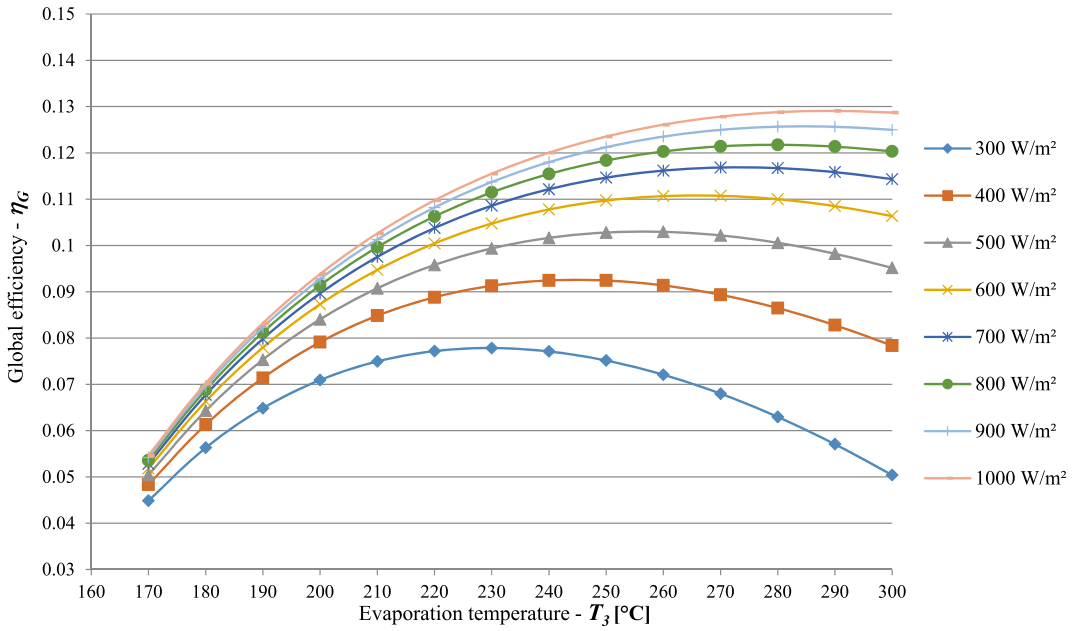

FIGURE 12 Solar-to-electricity efficiency vs vaporization temperature when condensation pressure is fixed at 100 kPa under growing solar irradiance intensity

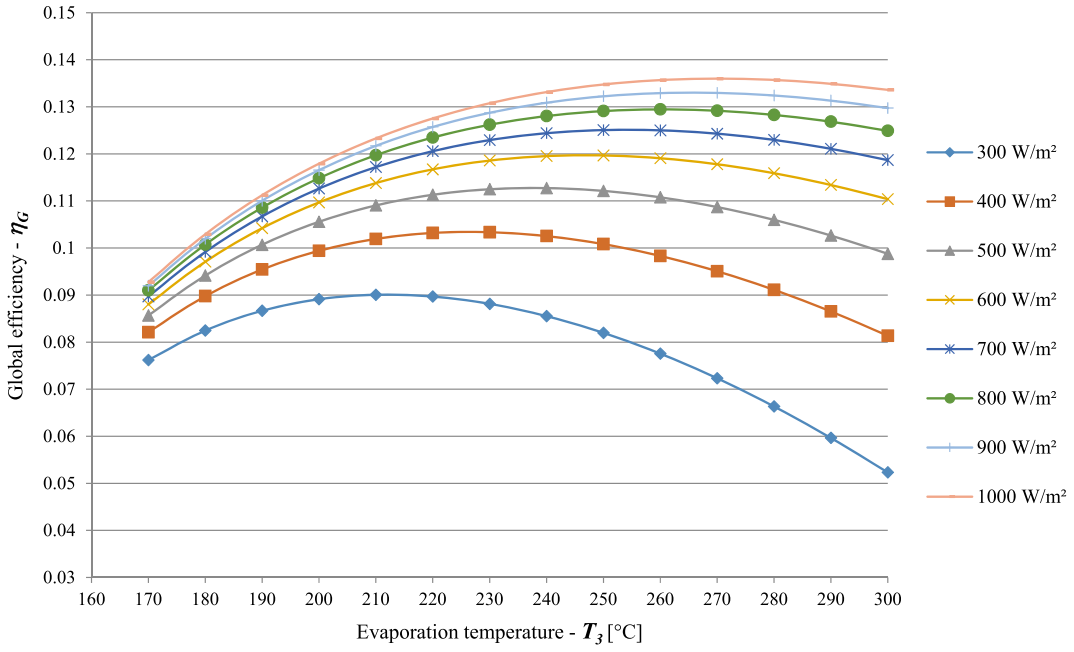

FIGURE 13 Solar-to-electricity efficiency vs vaporization temperature when condensation pressure is fixed at 50 kPa under growing solar irradiance intensity

reveal a prevalent decreasing trend as vaporization temperature increases. Indeed, Figure 14 shows that low vaporization temperatures lead to nearly constant or lightly lower overall energy conversion efficiency η_G in comparison with its maximum levels due to slightly lower steam Rankine cycle efficiency with a decreasing vaporization temperature (as described in Figure 11 when condensation pressure p_4 is fixed at 10 kPa).

However, it is manifest in these figures that, for every condensation pressure level, the solar-to-electricity efficiencies η_G do not have a monotonic growing trend with evaporation temperature but, after reaching a maximum,

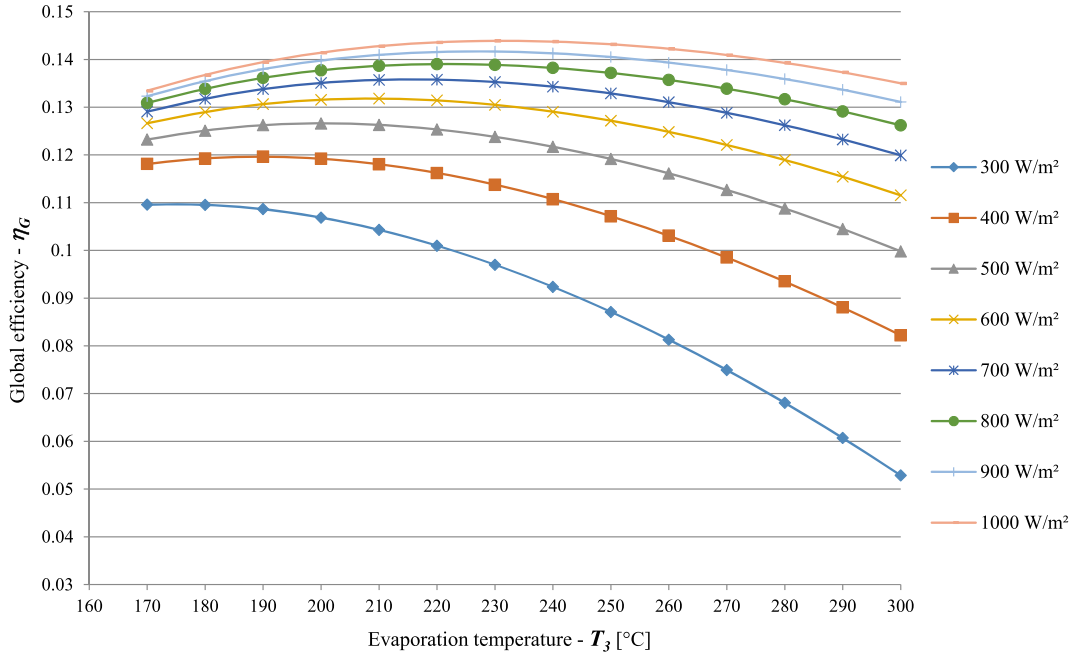

FIGURE 14 Solar-to-electricity efficiency vs vaporization temperature when condensation pressure is fixed at 10 kPa under rising solar irradiance intensity

they decrease for high vaporization temperature T_3. This is due to decreasing solar collector efficiencies η_{SOL} with increasing vaporization temperature (as exposed in Figure 8) which prevail over increasing Rankine cycle efficiencies η_{SRC}. For this reason, it is essential to detect optimum working conditions of the planned solar power plant for each level of solar irradiance intensity and condensation pressure.

Hence, with respect to each condensation pressure, to calculate the optimum evaporation temperatures that maximize the solar-to-electricity efficiencies η_G, the first derivative of each polynomial equation shown in Figures 12 to 14 were computed and set to zero. By following the above optimization procedure, which was developed with a specific MATLAB code based on the same parametric equations, the optimum vaporization temperatures $T_{3,op}$ and the ensuing maximum global efficiencies $\eta_{G,op}$ were detected for each solar irradiance intensity and condensation pressure, as presented in Figures 15 and 16, respectively.

In Figures 15 and 16 it is obvious that, for each level of condensation pressure, variations in both optimum vaporization temperatures and resulting maximum global efficiencies are monotonically growing functions of solar irradiance intensity G_b (rising from 300 to 1000 W/m^2). However, the results presented in Figure 16 clearly show that this SE-based DSG solar system attains its best energy performance for condensation pressure p_4 set to 10 kPa; in effect, the maximum solar-to-electricity efficiencies are reached when p_4 is equal to 10 kPa for each solar irradiance intensity. In fact, a growth in the attainable enthalpy of expansion as condensation pressure decreases from 100 to 10 kPa prevails over reduced efficiency of both screw expanders when over-expansion operating situations occur.[2] Therefore, in Figure 15 it is clear that, under a condensation pressure fixed to 10 kPa, the optimum vaporization temperatures $T_{3,op}$ range between 174°C and 232°C with increasing solar irradiance intensity from 300 to 1000 W/m^2, while the corresponding maximum global energy conversion efficiencies $\eta_{G,op}$ increase from 10.9% to 14.4% in the same solar irradiation range (Figure 16).

To better explain the energetic benefits of SC receivers when integrated in the proposed DSG power plant, a similar solar power plant, adopting SE as power machines and common PTC receivers as a thermal resource, was evaluated under the same working conditions. Thus, for a plant layout based on PTC receivers in place of SC receivers and by using the same parametric analysis, variations in solar-to-electricity efficiency η_G were calculated in the same ranges of evaporation temperature and solar irradiation intensity and for the same condensation pressure levels.[2]

As a result, if the less performing PTC receivers were adopted, the trend of the overall efficiency η_G against vaporization temperature would be very similar to that of solar power plants based on SC receivers. In particular, for a condensation pressure level equal to 10 kPa, the global efficiency should have a prevalent decreasing

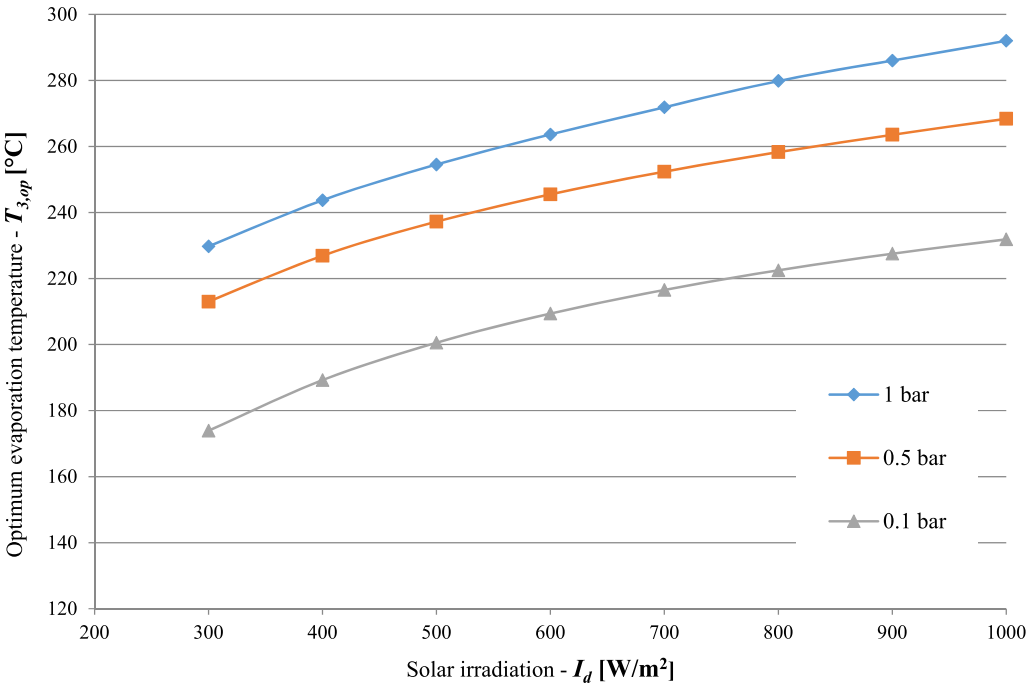

FIGURE 15 Optimum vaporization temperature calculated against solar irradiance intensity and condensation pressure

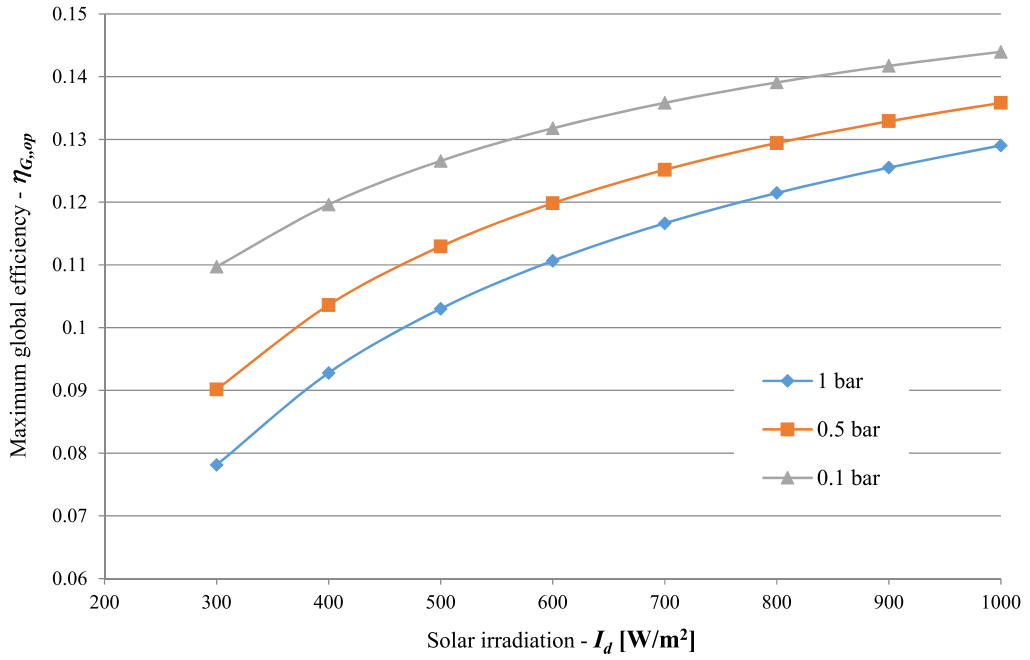

FIGURE 16 Best solar-to-electricity efficiency calculated against solar irradiance intensity and condensation pressure

trend as vaporization temperatures increase (as also shown in Figure 14 for Scheffler-based solar thermal electricity systems). In addition, for condensation pressure levels higher than 10 kPa, such global efficiencies should present a peak which can occur even at modest evaporation temperatures when solar irradiation intensities are lower than 600 W/m^2 (as also shown in Figures 12 and 13 for solar power plants based on Scheffler receivers).

The maximum global energy conversion efficiencies calculated for the PTC-based power plants were then compared in Figure 17 with those of the Scheffler-based solar thermal electricity system proposed in this research (already shown in Figure 16), in the same range of solar

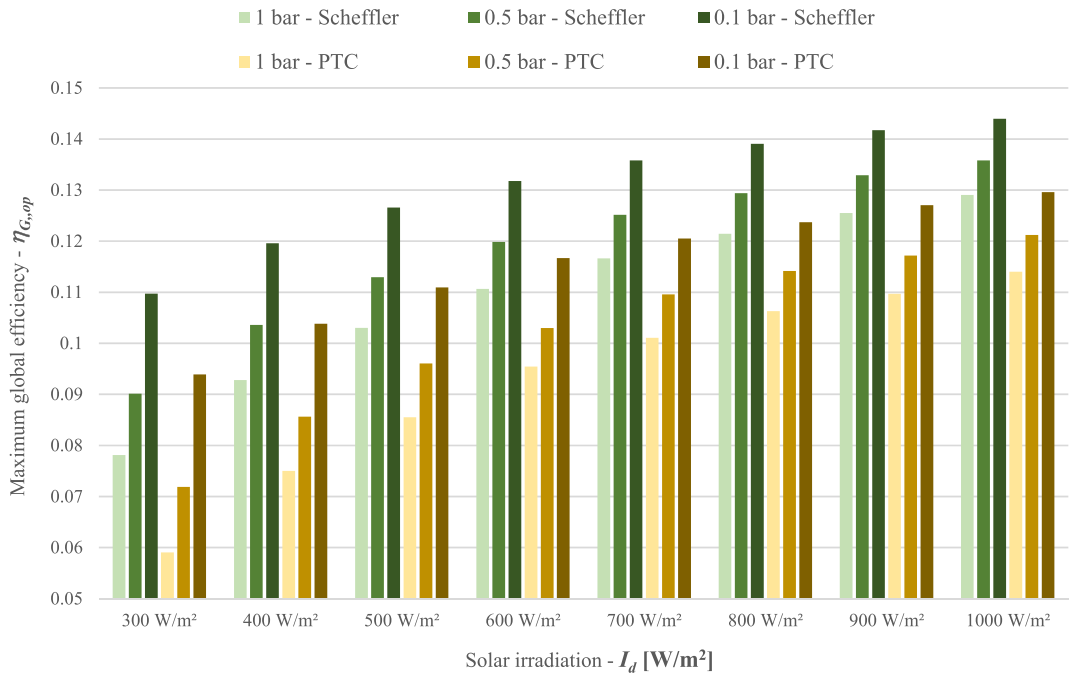

FIGURE 17 Best solar-to-electricity efficiencies calculated against solar irradiance intensity and condensation pressure: comparison between Scheffler and PTC receivers

irradiation intensity and for the same condensation pressure levels. Hence, in this figure it is clear that, for each level of condensation pressure, the highest efficiencies obtained by using the proposed Scheffler-based solar thermal electricity system at medium solar irradiance intensity (also below 600 W/m^2) can even reach the highest global energy conversion efficiencies achieved in PTC-based power systems under the maximum solar radiation (1000 W/m^2). This is due to the variability of the solar collector efficiency with solar radiation and evaporation temperature which is albeit slightly less wide for the SC receivers in comparison with PTC receivers (as already illustrated in Figures 8 and 9), thereby positively affecting the global solar-to-electricity efficiency of SC-based power plants.

Consequently, the proposed solar power plant based on SEs as power machines and SC receivers as a thermal resource, under the best working conditions established in this study, can work without reduction in global energy conversion efficiency in comparison with DSG solar thermal power systems adopting common parabolic trough collectors in place of SC receivers and dynamic expanders in place of SEs.

5 | CONCLUSIONS

This research aimed to develop a plant engineering idea of a small solar electricity generation system (10-100 kW) which could be easily used for civil applications due its simple construction, low cost, and minimal environmental impact. Basic principles were provided to assess the energy performance of an innovative CSP-SRC plant with direct steam generation, equipped with "Scheffler" solar receivers as a thermal source coupled with steam screw expanders as power machines. Parametric optimization of the planned solar power system was then achieved for different operating conditions of screw expanders with varying thermal power provided by the solar energy collection system. The proposed DSG power plant, under the established range of the optimum working situations, can work with energetic advantages in comparison with solar thermal power systems adopting parabolic trough collectors in place of SC receivers and dynamic expanders in place of SEs. Thus, power plants based on Scheffler solar receivers coupled with steam screw expanders can attract rising interest as advantageous sustainable solar power plants. The numerical results attained in this research are useful to deliver key procedures for the best harnessing of solar power in low-medium SE-based direct steam generation power plants equipped with Scheffler receivers, as well as for the further phase of the commercialization of this innovative system.

The key results of the energetic investigation established on the above solar thermal power system can be summarized as follows:

- SC receivers appeared to perform better than PTC receivers due to higher compactness of the focal

receiver compared to the linear collector of PTCs. The efficiency of SC receivers, in effect, remains sufficiently high even at high vaporization temperatures due to reduced convective and radiative heat losses. Besides, SC receivers are less sensitive to variations in solar irradiation intensity compared to PTC receivers.

- The proposed solar power plant, under the best working conditions established in this study, can work without reduction in global energy conversion efficiency in comparison with DSG solar thermal power systems adopting dynamic expanders in place of screw expanders.
- For each solar irradiance intensity, the maximum solar-to-electricity efficiencies are ensured when the condensation pressure is fixed to 10 kPa. Under this operating condition, the optimum vaporization temperatures $T_{3,op}$ range between 174°C and 232°C with increasing solar irradiance intensity from 300 to 1000 W/m^2, with the resulting maximum global energy conversion efficiency $\eta_{G,op}$ which increases from 10.9% to 14.4%.
- For each level of condensation pressure, the highest efficiencies obtained by using the proposed Scheffler-based solar thermal electricity system at medium solar irradiance intensity can even match the highest global energy conversion efficiencies achieved in PTC-based power systems under maximum solar radiation intensity.

ORCID

Paolo Iodice https://orcid.org/0000-0002-8660-7430
Francesco Saverio Marra https://orcid.org/0000-0003-4231-5652

REFERENCES

1. Masumn B-M, Masjuki H-H, Kalam M-A, Rizwanul Fattah I-M, Palash S-M, Abedin M-J. Effect of ethanol–gasoline blend on NOx emission in SI engine. *Renew Sust Energ Rev*. 2013;24:209-222.
2. Iodice P, Langella G, Amoresano A. Energy performance and numerical optimization of a screw expander–based solar thermal electricity system in a wide range of fluctuating operating conditions. *Int J Energy Res*. 2020;44(3):1858-1874.
3. Ganany A, Itay H. New design for CSP plant with direct-steam solar receiver and molten-salt storage. *AIP Conf Proc*. 2016;1734:060001. https://doi.org/10.1063/1.4949143
4. Sachdeva J, Singh O. Comparative evaluation of solarized triple combined cycle for different ORC fluids. *Renew Energy*. 2021;163:1333-1342.
5. Petrollese M, Cocco D. A multi-scenario approach for a robust design of solar-based ORC systems. *Renew Energy*. 2020;161:1184-1194.
6. Roumpedakis TC, Loumpardis G, Monokrousou E, Braimakis K, Charalampidis A, Karellas S. Exergetic and economic analysis of a solar driven small scale ORC. *Renew Energy*. 2020;157:1008-1024.
7. Mamun M-A-A, Biswas S. Waste heat recovery system by using an organic Rankine cycle (ORC). *Int J Sci Eng Res*. 2012;3(10):1-4.
8. Lin W, Nilsson L, Malutta R. Waste Heat Recovery by Organic Rankine Cycle (ORC) for Moist Exhaust Gases From Paper Industry. Paper presented at: ASME 2017 International Mechanical Engineering Congress and Exposition volume 6: energy Tampa, Florida, USA, November 3–9, 2017.
9. Shahverdi K, Loni R, Ghobadian B, et al. Energy harvesting using solar ORC system and Archimedes screw turbine(AST) combination with different refrigerant working fluids. *Energy Convers Manag*. 2019;187:205-220.
10. Darvish K, Ehyaei M-A, Atabi F, Rosen M-A. Selection of optimum working fluid for organic Rankine cycles by exergy and exergy-economic analyses. *Sustainability*. 2015;7:15362–15383.
11. Astolfi M. Techno-economic optimization of low temperature CSP systems based on ORC with screw expanders. Paper presented at: International Conference on Concentrating Solar Power and Chemical Energy Systems, SolarPACES. 2014
12. Li L, Sun J, Li Y, He YL, Xu H. Transient characteristics of a parabolic trough direct-steam-generation process. *Renew Energy*. 2019;135:800-810.
13. Li L, Sun J, Li Y. Thermal load and bending analysis of heat collection element of direct-steam-generation parabolic-trough solar power plant. *Appl Therm Eng*. 2017;127:1530-1542.
14. Price H, Lupfert E, Kearney D, et al. Advances in parabolic trough solar power technology. *J Sol Energy Eng*. 2002;124:109-125.
15. Li L, Li YS, Sun J. Prospective fully-coupled multi-level analytical methodology for concentrated solar power plants: applications. *Appl Therm Eng*. 2017;118:159-170.
16. Li L, Sun J, Li YS. Prospective fully-coupled multi-level analytical methodology for concentrated solar power plants: general modelling. *Appl Therm Eng*. 2017;118:171-187.
17. Laing D, Bahl C, Bauer T, Lehmann D, Steinmann WD. Thermal energy storage for direct steam generation. *Sol Energy*. 2011;85:627-633.
18. Montes M, Rovira A, Muñoz M, Martínez-Val J. Performance analysis of an integrated solar combined cycle using direct steam generation in parabolic trough collectors. *Appl Energy*. 2011;88:3228-3238.
19. Ruelas J, Velázquez N, Cerezo J. A mathematical model to develop a Scheffler-type solar concentrator coupled with a Stirling engine. *Appl Energy*. 2013;101:253-260.
20. Munir A, Hensel O, Scheffler W. Design principle and calculations of a Scheffler fixed focus concentrator for medium temperature applications. *Sol Energy*. 2010;84:1490-1502.
21. Oelher U, Scheffler W. The use of indigenous materials for solar conversion. *Sol Energy Mater Sol Cells*. 1994;33:379-387.
22. Stefanovic VP, Pavlovic SR, Bellos E, Tzivanidis C. A detailed parametric analysis of a solar dish collector. *Sustain Energy Technol Assess*. 2018;25:99-110.
23. Shubham, Kumar P, Kumar S, Kumar R, Mandal S. Numerical and experimental analysis of Scheffler concentrator receiver for steam generation using phase change material. *Int J Renew Energy Res*. 2018;8(3):1339-1345.
24. Tyroller M, Brücke S, Werdenbergstr G. Solar steam sterilizer for rural hospitals. Paper presented at: International Solar Cooker Conference. No. 34. Granada, Spain. 2006.

25. Chandak A, Somani S-K, Dubey D. Design, development of and testing of multieffect distiller/evaporator using Scheffler solar concentrator. *J Eng Sci Technol*. 2009;4:315-321.
26. Ramachandran S, Nene AA. Studies on Scheffler solar concentrator to optimise thermal efficiency. *Int J Ambient Energy*. 2020;1-8. https://doi.org/10.1080/01430750.2020.1805357
27. Iodice P, Langella G, Amoresano A. Modeling and energetic-exergetic evaluation of a novel screw expander-based direct steam generation solar system. *Appl Therm Eng*. 2019;155:82-95.
28. Fatigati F, Di Bartolomeo M, Cipollone R. Dual intake rotary vane expander technology: experimental and theoretical assessment. *Energy Convers Manag*. 2019;186:156-167.
29. Li J, Li P, Pei G, Alvi JZ, Ji J. Analysis of a novel solar electricity generation system using cascade Rankine cycle and steam screw expander. *Appl Energy*. 2016;165:627-638.
30. Li J, Li P, Gao G, Pei G, Su Y, Ji J. Thermodynamic and economic investigation of a screw expander-based direct steam generation solar cascade Rankine cycle system using water as thermal storage fluid. *Appl Energy*. 2017;195:137-151.
31. Read M, Stosic N, Smith I-K. Optimization of screw expanders for power recovery from low-grade heat sources. *Energy Technol Policy*. 2014;1:131-142.
32. Invernizzi C, Iora P, Silva P. Bottoming micro-Rankine cycles for micro-gas turbines. *Appl Therm Eng*. 2007;27:100-110.
33. Li P, Li J, Gao G, et al. Modeling and optimization of solar-powered cascade Rankine cycle system with respect to the characteristics of steam screw expander. *Renew Energy*. 2017;112:398-412.
34. Wang W, Wu Y-T, Ma C-F, Xia G-D, Wang J-F. Experimental study on the performance of single screw expanders by gap adjustment. *Energy*. 2013;62:379-384.
35. Tang H, Wu H, Wang X, Xing Z. Performance study of a twin-screw expander used in a geothermal organic Rankine cycle power generator. *Energy*. 2015;90:631-642.
36. Li P, Li J, Tan R, et al. Thermo-economic evaluation of an innovative direct steam generation solar power system using screw expanders in a tandem configuration. *Appl Therm Eng*. 2019;148:1007-1017.
37. Reddy D-S, Khan M-K, Alam M-Z, Rashid H. Design charts for Scheffler reflector. *Sol Energy*. 2018;163:104-112.
38. Duffie J-A, Beckman W-A, Worek W-M. *Solar Engineering of Thermal Processes*. New York, NY: Wiley; 2013.
39. Dib E-A, Fiorelli F-A. Analysis of the image produced by Scheffler paraboloidal concentrator. Paper presented at: 5th International Youth Conference on Energy (IYCE) (pp. 1–7). IEEE May 2015.
40. Stine WB, Harrigan RW. *Solar Energy Fundamentals and Design with Computer Applications*. New York, NY: Wiley-Interscience; 1985.
41. Shuai Y, Xia X-L, Tan H-P. Radiation performance of dish solar concentrator/cavity receiver systems. *Sol Energy*. 2008;82:13-21.
42. Fraser P-R. Stirling Dish System Performance Prediction Model, MSc Thesis, University of Wisconsin-Madison. 2008.
43. Hogan P-A, Fane A-G, Morrison G-L. Desalination by solar heated membrane distillation. *Desalination*. 1991;81:81-90.
44. Ayres F-J. *Differential and Integral Calculus*. Madrid España: Schaum; 1989.
45. Abramowitz M, Stegun I-A. *Handbook of Mathematical Functions: With Formulas, Graphs, and Mathematical Tables, National Bureau of standards applied mathematics series 55*. Tenth Printing. Washington, D.C.: U.S. Government Printing Office; 1972.
46. Azzouzi D, Boumeddane B, Abene A. Experimental and analytical thermal analysis of cylindrical cavity receiver for solar dish. *Renew Energy*. 2017;106:111-121.
47. Stine W-B, McDonald C-G. Cavity Receiver Convective Heat Loss. Paper presented at: International Solar Energy Society. Solar World Congress: Kobe, Japan. 1989.
48. Harris J-A, Lenz T-G. Thermal performance of solar concentrator/cavity receiver systems. *Sol Energy*. 1984;34:135-142.
49. Ma R-Y. Wind effects on convective heat loss from a cavity receiver for a parabolic concentrating solar collector (No. SAND-92-7293). Sandia National Labs., Albuquerque, NM (United States); California State Polytechnic Univ., Pomona, CA (United States). Dept. of Mechanical Engineering. 1993.
50. Incropera F-P, DeWitt D-P, Bergman T-L, Lavine A-S. *Fundamentals of Heat and Mass Transfer*. Hoboken, NJ: John Wiley & Sons. Inc; 2002.
51. Tian Y, Xing Z, He Z, Wu H. Modeling and performance analysis of twin-screw steam expander under fluctuating operating conditions in steam pipeline pressure energy recovery applications. *Energy*. 2017;141:692-701.
52. Iodice P, Langella G, Amoresano A. Direct steam generation solar systems with screw expanders and parabolic trough collectors: Energetic assessment at part-load operating conditions. Case Studies in Thermal Engineering. 2020;19. art. no. 100611.
53. Iodice P, Langella G, Amoresano A. Exergetic analysis of a new direct steam generation solar plant using screw expanders. *Energies*. 2020;13:720.
54. Diver RB, Andraka CE, Scott RK, Goldberg V, Thomas G. The advanced dish development system project. Paper presented at: Proceedings of solar forum; April 21, 2001. Washington, DC, USA; 2001. p. 1–6.
55. Reinalter W, Ulmer S, Heller P, et al. Detailled performance analysis of the 10 kW CNRS-PROMES dish/Stirling system. Paper presented at: Proceedings of the 13th SolarPACES international symposium, 2006, Seville Spain; 2006. A7–S7 p. 1–9.
56. Avadhanula VK, Lin C-S. Empirical models for a screw expander based on experimental data from organic Rankine cycle system testing. *J Eng Gas Turbines Power*. 2014;136:062601.
57. Ng K, Bong T, Lim T. A thermodynamic model for the analysis of screw expander performance. *Heat Recovery Syst CHP*. 1990;10:119-133.

How to cite this article: Iodice P, Amoresano A, Langella G, Marra FS. Combined use of volumetric expanders and Scheffler receivers to improve the efficiency of a novel direct steam solar power plant. *Int J Energy Res*. 2021;1-24. https://doi.org/10.1002/er.7163